Satellite-based Sea Surface Salinity designed for Ocean and Climate Studies

J. Boutin[1], N. Reul[2], J. Koehler[3], A. Martin[4], R. Catany[5], S. Guimbard[6], F. Rouffi[7], J.L. Vergely[7], M. Arias[5], M. Chakroun[7], G. Corato[8], V. Estella-Perez[1,*], A. Hasson[1,†], S. Josey[4], D. Khvorostyanov[1], N. Kolodziejczyk[2], J. Mignot[1], L. Olivier[1], G. Reverdin[1], D. Stammer[3], A. Supply[1,2], C. Thouvenin-Masson[1], A. Turiel[9], J. Vialard[1], P. Cipollini[10, ‡], C. Donlon[10, ‡], R. Sabia[11], S. Mecklenburg[10]

[1]Sorbonne University, LOCEAN/IPSL Laboratory, CNRS–IRD–MNHN, Paris, France.

[2]University of Brest, LOPS Laboratory, IUEM, UBO–CNRS–IRD–Ifremer, Plouzané, France.

[3]Institut für Meereskunde, Centrum für Erdsystemwissenschaften und Nachhaltigkeit, Universität Hamburg, Germany.

[4]National Oceanography Centre, Southampton, UK.

[5]ARGANS Ltd, UK.

[6]Ocean Scope, France.

[7]ACRI-st, France.

[8]Adwaiseo, Luxemburg.

[9]Barcelona Expert Center (BEC) and Institute of Marine Sciences (ICM), CSIC, Spain.

[10]European Space Agency, ECSAT, Harwell, United Kingdom.

[11]Telespazio-UK for ESA, ESRIN, Frascati, Italy.

Corresponding author: Jacqueline Boutin (jb@locean.ipsl.fr)

*Now at UL Services Spain SL

†Now at Mercator Ocean International, France

‡Now at European Space Agency, ESTEC, Noordwijk, the Netherlands.

Key Points:

- 2010-2019 sea surface salinity fields built from three satellite missions data sets
- Monitors sea surface salinity variability at large meso- to basin scale with unprecedented accuracy and spatio-temporal coverage
- Answers the need for Sea Surface Salinity global fields at higher resolution than 1 month, 1°

Abstract

Sea Surface Salinity (SSS) is an increasingly-used Essential Ocean and Climate Variable. The SMOS, Aquarius, and SMAP satellite missions all provide SSS measurements, with very different instrumental features leading to specific measurement characteristics. The Climate Change Initiative Salinity project (CCI+SSS) aims to produce a SSS Climate Data Record (CDR) that addresses well-established user needs based on those satellite measurements. To generate a homogeneous CDR, instrumental differences are carefully adjusted based on in-depth analysis of the measurements themselves, together with some limited use of independent reference data. An optimal interpolation in the time domain without temporal relaxation to reference data or spatial smoothing is applied. This allows preserving the original datasets variability. SSS CCI fields are well-suited for monitoring weekly to interannual signals, at spatial scales ranging from 50 km to the basin scale. They display large year-to-year seasonal variations over the 2010-2019 decade, sometimes by more than +/-0.4 over large regions. The robust standard deviation of the monthly CCI SSS minus *in situ* Argo salinities is 0.15 globally, while it is at least 0.20 with individual satellite SSS fields. r^2 is 0.97, similar or better than with original datasets. The correlation with independent ship thermosalinographs SSS further highlights the CCI dataset excellent performance, especially near land areas. During the SMOS-Aquarius period, when the representativity uncertainties are the largest, r^2 is 0.84 with CCI while it is 0.48 with the Aquarius original dataset. SSS CCI data are freely available and will be updated and extended as more satellite data become available.

Plain Language Summary

Salinity measures the mass of dissolved salts in seawater. Together with temperature and pressure, it determines the seawater density, which is crucial in driving oceanic motions. Low sea surface salinity (SSS) can be the result of freshwater inputs such as rain, river runoffs, and ice melt. In contrast, high SSS often characterize regions of strong evaporation. The salinity imprint of these processes is then carried by ocean currents over long distances and long periods of time. SSS also impacts ocean circulation through its effect on density, and modulates ocean-atmosphere exchanges of heat and gases. SSS is a hence key variable for ocean and climate studies, both as a passive tracer and as an important actor of oceanic processes.

Since 2010, three satellite missions have monitored SSS with an unprecedented spatial and temporal resolution. For the first time, data from these satellites are combined, taking each instrument specific features into account. The resulting dataset enables global SSS to be monitored and studied with unprecedented accuracy over the 2010-2019 period, at a 50km, weekly or monthly resolution. It reveals large SSS signals related to phenomena affecting climate in various parts of the world ocean.

1 Introduction

Salinity is a key ocean and climate variable that plays a fundamental role in the thermohaline global ocean circulation, the hydrological cycle, and climate variability (Durack et al., 2012; Siedler et al., 2001).

Along with temperature, salinity controls sea water density. This parameter influences the ocean stratification, water mass formation, and ultimately the general circulation of the ocean. At high latitudes, in cold polar surface waters (typically Sea Surface Temperature (SST)= 2°C), a change of 0.11 in Sea Surface Salinity [1,2] (SSS), is equivalent, in terms of density, to a change of 1°C in SST. In warm regions (SST=28°C), a larger salinity change of 0.44 is equivalent to a 1°C change in SST, as per its density contribution. This is the reason why salinity variations play a key role in controlling the global thermohaline circulation, in particular due to high salinities anomalies strongly contributing to convective overturning (i.e. transporting waters from the ocean surface to the deep ocean) at high latitudes. It is also a tracer of oceanic processes (advection, mixing). SSS bears the signature of freshwater fluxes originating from evaporation minus precipitation (E-P), river discharges and ice melting or freezing. Freshwater fluxes can modify the vertical stratification in density and strongly influence the air-sea exchange through the development of so-called salt-stratified (halocline) barrier layers (Lukas and Lindstrom, 1991). Indirectly, salinity contributes to El-Nino Southern Oscillation (ENSO) (Vialard and Delecluse, 1998), Indian Monsoon (Shenoi et al., 2002) and primary productivity (Picaut et al.,

[1] Sea Surface Salinity in this article refers to the salinity determined from a satellite microwave radiometer sensing the thermal emission at 1.4GHz due to its changing dielectric properties. Thus the measured quantity is representative of the upper few cm of the sea surface depending on the depth of surface foam present on the sea surface.

[2] Sea Surface Salinity is expressed with no physical units. It is defined according to the Practical Salinity Scale (UNESCO, 1985) as conductivity ratio: a seawater sample of Practical Salinity 35 has a conductivity ratio of 1.0 at 15°C and 1 atmosphere pressure, using a potassium chloride (KCl) standard solution containing a mass of 32.4356 grams of KCl per Kg of solution.

2001). At high latitude, the sharp halocline shields the heat stored in the deep ocean from reaching the surface layer and melting the sea ice (Carmack et al., 2016; Lique, 2015; Steele et al., 2004).

The ocean is a major component of the Earth's water cycle: 86% of evaporation and 78% of precipitation take place over the ocean. The near-surface salinity also carries the imprint of the anthropogenic influence on water cycle, with a tendency for SSS to increase in evaporation regions and decrease in precipitation-dominated regions (Yu et al., 2020). This so-called observed 'dry gets dryer and wet gets wetter' tendency also occurs in climate models projections (Bindoff et al., 2019). Both positive and negative trends in ocean salinity and freshwater content have been observed throughout much of the ocean including sea surface and ocean interior, providing indirect evidence that the E – P pattern over the oceans is amplifying. In addition, evaporated water above the ocean is transported above the continents by atmospheric circulation. Li et al. (2016) recently found correlations between satellite SSS anomalies in the North Atlantic and anomalies of rain in Sahel lagged by several months suggesting that large-scale SSS anomalies could bring skill as precursor indicators of rain over the continents.

In addition, being the total mass of dissolved salts per kg of seawater, salinity affects the entire oceanic carbonate system and its components: total alkalinity, dissolved inorganic carbon, pH, and fugacity of CO_2 (Millero, 2007).

Due to its role both as a variable that influences the oceanic circulation, air-sea exchanges, upper-ocean biogeochemical state and as a tracer of the water cycle and its changes, SSS has been identified as an Essential Climate Variable (ECV) (https://public.wmo.int/en/programmes/global-climate-observing-system/essential-climate-variables).

SSS measurement by satellite remote sensing was motivated by the essential need for better monitoring, understanding and constraining the marine components of the climate system. At the end of the 1990s, the Global Ocean Data Assimilation Experiment (GODAE) group estimated that it was necessary to measure SSS with an accuracy of 0.1 at monthly, 100 km (or every 10 days at 200 km) scales. Since the beginning of the 21st century, the Argo network of in-situ profiling floats has continuously evolved (Roemmich et al., 2019) and provided invaluable measurements of 3D oceanic salinity. The Argo array reached global coverage in 2006 with one

measurement of both temperature and salinity every ~10 days and every ~300 km with a vertical sampling range of between about 5 - 2000m depth. Nevertheless, there is increasing consensus that the GODAE specifications that are well covered by the Argo network do not serve all the needs for ocean and climate studies. The analysis of ship measurements (Delcroix et al., 2005), and later of satellite measurements have revealed a natural variability of SSS much larger than 0.1 in regions characterized by large mesoscale variations (Fournier et al., 2016; Hasson et al., 2019; Reul et al., 2014), in river plumes and areas characterized by strong precipitation events (e.g., Figure 6 in Boutin et al. 2016). In these regions, SSS fields derived from satellite data depict SSS variability much better than the salinity products derived from the in situ Argo network alone (Fournier and Lee, 2021).

Satellite SSS data are available with regular repeat global coverage since 2010, thanks to to microwave radiometers operating at a frequency of 1.4 GHz (wavelength 21 cm; L-Band). The brightness temperature (Tb) measured by ocean-observing microwave radiometers is related to the emissivity of the ocean surface layer. The L-Band Tb depends primarily on the dielectric properties of the surface seawater (i.e., seawater conductivity and, thus, salinity and temperature) and its geometric characteristics, determined by sea surface roughness (Reul et al., 2020). At this frequency, the atmosphere is almost transparent (except for strong precipitation). Molecular oxygen has the most significant effect on the measured Tb with small contributions from water vapor, cloud liquid water, and rain. Tb has a relatively low sensitivity to SSS, especially at low SST: the Tb change per SSS unit is ~0.8 K at 30°C and ~0.2 K at 0°C (Yueh et al., 2001). The radiometer measurements of SSS in cold waters at high latitudes are thus particularly challenging.

SSS measured from satellites is not directly comparable to near surface in-situ measurements due to the vertical structure of salinity in the upper ocean. At L-Band in foam-free conditions, the emissive ocean surface layer is ~1cm deep (when the foam is present, emissions may emanate from a layer >5 cm thick (Anguelova and Gaiser, 2011)), while the upper measurements performed by most in-situ devices (such as Argo floats, thermosalinograph onboard ships, or moorings networks) are in the depth range of 1 to 20 m. Obtaining high vertical resolution measurements in the upper few meters of the ocean is particularly challenging – even when using all available in-situ data sources. Hence, significant differences between satellite SSS compared to in-situ salinity have been observed with mean vertical differences

larger than 0.1 in the Pacific, Atlantic, and Indian Oceans coinciding with the average position of the inter-tropical convergence zone (ITCZ) heavy precipitations. The upper ocean stratification effects are the subject of dedicated experiments and their quantification via air-sea coupling modeling an active research domain (e.g. (Drushka et al., 2019) and references herein). Furthermore, L-band satellite measurements are integrated over a large spatial footprint, from ~40 km to more than 100 km, which poses obvious representativity issues when compared to punctual samples from Argo floats or ship transects. These issues have a strong impact when using in situ data for validation and vicarious calibration of satellite SSS products which must be managed with care in these areas of potentially significant vertical salinity stratification.

In the open ocean, the uncertainty of the SMOS (Soil Moisture and Ocean Salinity), Aquarius, and SMAP (Soil Moisture Active Passive) satellite SSS averaged over the GODAE scales is now estimated to be of the order of 0.2 (Reul et al., 2020; Vinogradova et al., 2019). SMOS data initially suffered from large systematic errors in the vicinity of the coast and in areas polluted by radio frequency interferences (RFI). SMAP data are less polluted than SMOS in these areas because of advanced RFI filtering capabilities. However, recent SMOS processing largely reduces these systematic errors making SMOS SSS often very close to SMAP SSS (e.g. (Akhil et al., 2020; Fournier and Lee, 2021)).

As this study started, individual satellite SSS is capable of resolving the upper register of the mesoscale spectrum (spatial scale of 50-500 km and temporal scale of 10-100 days) (e.g (Hasson et al., 2019; Huang et al., 2021; Kolodziejczyk et al., 2021; Lin, 2019; Melnichenko et al., 2021; Olivier et al., 2020)). These scales play an important role in the mixing and exchanges of water masses close to fronts, as a result of ocean circulation and atmospheric fluxes. At larger scales, ENSO events in the tropical Pacific have serious climatic repercussions at planetary scale and are the main source of interannual climatic variability with strong societal consequences (agriculture, marine ecosystems, health…) in many areas (McPhaden et al., 2006). We list below progresses which have been allowed by satellite SSS data. Zhu et al. (2014) have shown that salinity variability may play an active role in ENSO evolution, and is thus an important information to be taken into account for a better understanding of air-sea interaction processes during ENSO. Furthermore, monitoring ENSO phases via dedicated SSS-based climate indexes is useful to complement existing SST-based indexes (Qu and Yu, 2014). There is also some recent evidence that SSS provides an additional forecast skill for ENSO prediction (Hackert et

al., 2020). Given the scientific advances made possible by satellite-based SSS, the redefinition of the observation strategy in the tropical Pacific Ocean (Cravatte, 2016) and in the tropical Atlantic ocean (Foltz et al., 2019) underlined the need to pursue SSS satellite measurements.

Variations of precipitations above continents lead to variations of river discharges (Amazon/Orinoco, Congo, Niger, Mississippi…) which, together with ocean circulation, lead to a large SSS variability in river plumes. These have been well observed and documented by SMOS, Aquarius, and SMAP measurements in the tropics (e.g. (Akhil et al., 2020; Fournier et al., 2016; Houndegnonto et al., 2021; Reverdin et al., 2021) and references herein).

Furthermore, SMOS and SMAP data analysis have shown that the active role of the salinity in the development of barrier layers might intensify the water cycle in some tropical areas. Under tropical cyclones, it limits vertical mixing and hence cooling of the ocean surface which influences the development of the cyclones themselves (Balaguru et al., 2020; Reul et al., 2021). These SSS feedbacks on climate are of increasing importance for climate studies.

Satellite SSS provides a precious information to better understand and constrain the air-sea CO_2 exchanges, due to the dependency of carbonate properties on seawater salinity. Satellite SSS is in particular useful to study the total alkalinity and pH (Fine et al., 2017; Land et al., 2015; Salisbury et al., 2015).The impact of fresh water input onto air-sea CO_2 exchanges has been highlighted from satellite data in high precipitation regions (Brown et al., 2015; Ho and Schanze, 2020) and in river plumes (Ibánhez et al., 2017; Lefèvre et al., 2014).

The goal of the European Space Agency (ESA) Climate Change Initiative Sea Surface Salinity (CCI+SSS) project is to optimize satellite SSS time series by merging satellite SSS acquired by various instruments. For the first time, SMOS, Aquarius, and SMAP measurements are combined to produce Level 4 (L4) gridded multi-mission estimates of SSS. Such a combination reduces the noise of satellite SSS fields owing to better sampling and improves the spatial resolution of large mesoscale SSS features. Examples of the derived merged SSS L4 maps are illustrated in Figure 1 during a period with SMOS data-only, a period with SMOS plus Aquarius data and a period with SMOS plus SMAP SSS measurements. The large mesoscale features around tropical river plumes (e.g., Amazone, Orinoco, Congo), frontal regions (e.g. Gulf Stream) are nicely captured by the satellite products. The addition of SMAP SSS leads to a reduced noise during the SMOS and SMAP period with respect to the SMOS-only period, and to

a reduced blurring with respect to the SMOS-Aquarius period, owing to the better spatial resolution of SMOS and SMAP compared to Aquarius.

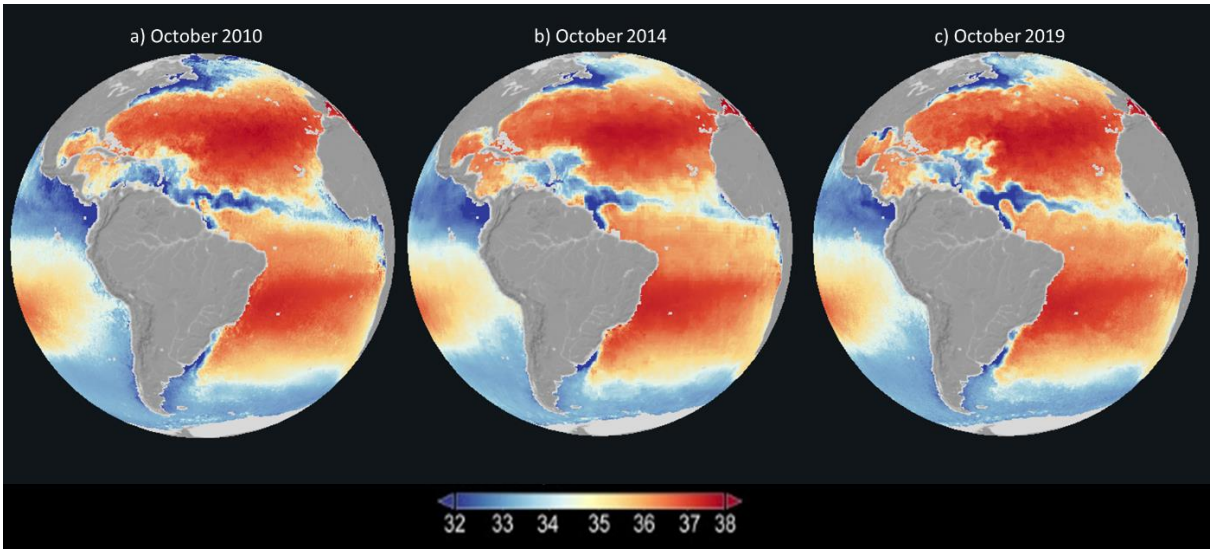

Figure 1: Example of CCI L4 satellite SSS fields in October a) 2010 (SMOS only period), b) 2014 (SMOS and Aquarius period) and c) 2019 (SMOS and SMAP period). (CCI monthly maps from the ESA Climate from Space website https://cfs.climate.esa.int)

We have polled potential users of the CCI+SSS product using a Web Survey (available at https://forms.gle/BVDroYrNpVvpxFJu9), in order to better define their needs. A more detailed overview of the results of this poll can be found in the supporting information S1, but we briefly summarize the main points here. Most users were interested by global L4 products that cover a period of at least 9 years, with a typical resolution of 1 day to 1 month and 0.25 to 1°. In fact, there appear to be both the need for high-resolution, low accuracy (weekly 0.25° ~ 0.3) and lower-resolution higher accuracy (montly 1°, < 0.1) products. Users also request some simple characterization of the quality of the data, along with its value. Finally, many users thought that it was important to merge SSS datasets from several sources. In this paper, we address the merging of several satellite products, also using a limited statistical information about SSS variability derived from in situ and model reanalyses.

The objective of this paper is to describe the method and data employed to build the CCI L4 SSS time series, and then the ones used in the validation exercise; to analyze the resulting fields and their validity; to review and discuss the strength of satellite merged SSS and its remaining caveats and propose research avenues to solve or mitigate them.

2 Data and Methods: CCI L4 SSS

2.1 Overview

The CCI+SSS algorithm described in this paper corresponds to the version 2 of the algorithm. It is summarized in Figure 2 and in this subsection, with each step and dataset more thoroughly described in the remaining of section 2.

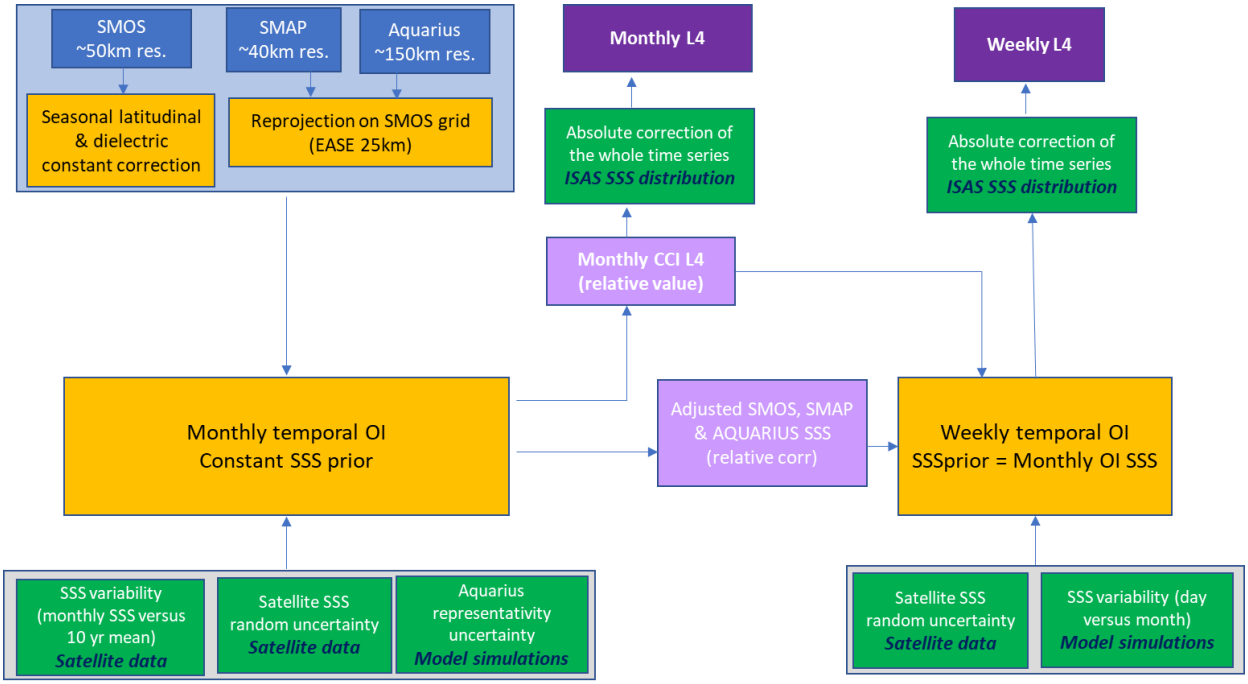

Figure 2: Outline of the CCI+SSS merging methodology which is performed independently on each node of the EASE 25km grid. Input satellite SSS data are indicated in light blue boxes, additional input information is in green boxes (origin of this information in bold black), processing steps are in yellow boxes, temporary informations output of monthly OI are in light violet boxes and output CCI+SSS L4 fields are in violet boxes.

The main inputs are the satellite datasets. The SMOS input data has the same rectangular 25km Equal-Area Scalable Earth (EASE) 2.0 grid than our final CCI SSS dataset. The SMAP and Aquarius datasets are all reprojected on the same grid. The spatial resolution of each level 4 SSS is driven by the spatial resolution of the SMOS and SMAP SSS measurements, i.e. ~50 km x 50 km. Most of the input datasets biases are treated in the optimal interpolation (OI) step (see below). The input datasets hence simply undergo a minimal level of pre-processing of well known biases. This includes a better model of the dielectric constant and a correction for seasonal latitudinal biases for SMOS (see section 2.2 for more details). Seasonal latitudinal biases are corrected in the SMAP original processing and are neglected in case of Aquarius. The latter could be revised in a future version.

The monthly CCI SSS maps are obtained based on an OI in the time domain, i.e. each grid point is treated separately, the intent being to preserve the spatial SSS features contained in the original datasets. A larger representativeness error is attributed to Aquarius to account for the fact that its effective resolution is lower than that of SMAP and SMOS. The a-priori value of the SSS is set to a constant value, the median of the observed SSS over the full time period. The OI is performed over the entire time period of the three datasets.

The errors on the input satellite datasets to be corrected during the OI include:

- Poorly modeled instrumental effects (solar influence, land contamination, absolute calibration …),
- Radiometric noise,
- Flaws in the radiative transfer model (e.g. deficiencies in rough sea surface emission, in scattering of galactic and solar radiation…),
- Uncertainty in auxiliary geophysical data used as priors in the retrieval algorithms (wind speed, SST…),
- Measurement contamination by spurious effects (e.g. RFI).

Both a random component and a systematic component of the error in each dataset are estimated by the OI. The systematic component (also called bias) depends on each satellite measurements geometry: it is constant in time but highly variable in space (for instance it tends to be higher near coasts where RFI and pollution by land signals are more common).

The OI relies on error statistics to estimate these two components of the error. These statistics include the error variance which is deduced from the data itself (see section 2.4.2) and a temporal covariance. The bias correction is nonlocal (it uses the entire time period of the three datasets), while the random part is treated more locally. A theoretical estimate of random uncertainty associated with the CCI L4 SSS product is provided by the OI.

The previous OI step is meant to combine the various datasets into a consistent one, but a final calibration of the absolute reconstructed SSS is still needed. This is done by adjusting the median value (or the upper quartile in highly variable regions, see section 2.3.1) of the multi-satellite SSS to that of the ISAS product, reconstructed from in situ data.

The weekly data is obtained through another OI, but this time using as inputs the satellite SSS corrected from the systematic uncertainties estimated by the monthly OI, using the monthly data as an a priori value and using a representativity uncertainty between monthly and weekly SSS derived from an ocean model reanalysis.

In the following, we present the satellite datasets and the auxiliary datasets used in the OI. We then describe the OI method and the methodologies followed to derive the various components (such as the error statistics) involved in the OI.

2.2 Input Satellite Data

The main characteristics of L-band radiometric satellite missions enabling global SSS measurements are summarized in Table 1.

Table 1. Missions characteristics

SMOS MISSION	**AQUARIUS MISSION**	**SMAP MISSION**
-L-band interferometry. 0°-~60° earth incidence angles -revisit times: 4 days -resolution: about 50 km -repeat sub-cycle: 18 days -see more in (Font et al., 2010; Y. Kerr et al., 2010)	-L-band real-aperture radiometer. 3 fixed beams at 28.7, 37.8, and 45.6° earth incidence angles -revisit times: 7 days -resolution: about 150 km -repeat cycle: 7 days -see more in (Lagerloef et al., 2008)	-L-band real-aperture radiometer. Conical scanning, 40° earth incidence angle -revisit times: 3 days -resolution: about 40 km -repeat cycle : 8 days -see more in (Piepmeier et al., 2017)

We consider the longest SMOS, SMAP, and Aquarius SSS retrieved with up-to-date algorithms available at the time of the development of the CCI L4 SSS (Table 2).

Table 2. Satellite SSS products used to derive CCI L4 SSS fields.

SMOS SSS	Jan. 2010- Nov. 2019 L2P CATDS from ESA v622 algorithms (CATDS, 2017) Seasonal latitudinal correction SST correction derived from (Dinnat et al., 2019)
SMAP SSS	Apr. 2015 – Nov. 2019 L2C v4.0 RemSS (Meissner et al., 2019) Flagging as recommended in the user guide. Reprojection on 25 km EASE grid using nearest neighbor criteria.
AQUARIUS SSS	Aug. 2011 – June 2015 L3 daily products (Ascending & Descending orbits separated) (Meissner et al., 2018) Nearest neighbor colocation applied to 25 km EASE grid pixels falling within a 1°x1° Aquarius pixel.

SMOS data are internally generated by the *Centre Aval de Traitement des Données SMOS* (CATDS), the so-called L2P products based on SMOS ESA L2 v622 algorithm (Arias and SMOS_Ocean_Expert_Support_Laboratories, 2016). We summarize below the main processing steps; detailed information about the processing and the filterings is reported in Supporting information S2. Dinnat et al. (2019) found systematic errors of SMOS SSS as a function of SST that are attributed to deficiencies of the Klein and Swift (1977) dielectric constant model at extreme SST values. This leads us to adjust SMOS SSS with a polynomial SST function. A correction for seasonal latitudinal varying biases (e.g. those linked to solar or galactic effects) is also applied, similar to what is described in (Boutin et al., 2018):

$$SSS_{obs}(t, \phi, \lambda, x_{swath}, x_{orb}) = SSSsmos_{ref}(\phi, \lambda, m) - b_{lat}(\phi, x_{swath}, x_{orb}, m) \quad (1)$$

where SSS_{obs} is the observed SSS, t is the time of the measurement, ϕ, and λ, are respectively the latitude and the longitude of the considered pixel over the ocean, x_{swath} corresponds to the pixel location across the swath, x_{orb} indicates the satellite orbit direction (ascending or descending), b_{lat} is a latitudinal correction that varies seasonally as a function of the month, m, and $SSSsmos_{ref}$ is a reference SMOS SSS taken at a given x_{swath} and x_{orb}. In order to avoid land-sea contamination, b_{lat} is derived from SMOS measurements at several hundred

kilometers from coast. b_{lat} is removed from all SMOS SSS whatever their distance to coast and before estimating the temporally constant land-sea contamination correction (section 2.4.4). Actually, the seasonal latitudinal bias is expected to affect all pixels, whatever their distance to land.

SMAP v3 and Aquarius v5 SSS retrieval algorithms are described in (Meissner et al., 2018). SMAP algorithm has been updated towards version 4 as described in Meissner et al. (2019) with improved land correction, sea-ice mask, ice flagging. SMAP and Aquarius SSS are reprojected on the SMOS CATDS spatial grid, the rectangular EASE 2.0 grid (Brodzik et al., 2012) with 625 km^2 surface resolution (referred to as 25km EASE grid in this paper) using the nearest neighbor criterion. We do not apply seasonal latitudinal correction to SMAP SSS as the reflector emissivity correction (Table 1) already ensures latitudinal seasonal consistency with Argo. Seasonal latitudinal biases are neglected for Aquarius SSS because they are smaller than SMOS ones. They could however be considered in future CCI+SSS versions as Kao et al. (2018) and Meissner et al. (2018) found latitudinal seasonal SSS systematic differences with respect to Argo SSS or between ascending and descending passes that can reach +/-0.2.

RFI and calibration stability are two main challenges to deal with before retrieving reliable SSS measurements, given the low sensitivity of Tb to salinity (0.5K per salinity unit at 20°C at nadir). The data processing for each satellite mission is summarized below.

SMOS, Aquarius, and SMAP missions operate in a protected spectrum band (1400-1427 MHz) that is nevertheless known now to be affected by numerous RFI. Areas affected by RFI might experience data loss or result in inaccurate salinity retrieved values. To alleviate this situation, several strategies were set up to filter RFI contaminated measurements. SMOS, launched in 2009, was the first satellite with a radiometer operating in L-band, and it does not have any on-board hardware/software to filter RFI, so that RFI counteracting only relies on data post-acquisition processing. Filtering is significantly improved for SMAP (Soldo et al., 2019) (and to a lesser extent for Aquarius (Le Vine and Matthaeis, 2014)), as they are (were) equipped with on-board frequency/time-domain-based RFI filters. Nonetheless, RFI remains a major problem (e.g. (Kristensen et al., 2019)).

Onboard calibration and correction for parasitic effects does not allow to reach enough Tb stability and accuracy to cope with the SSS remote sensing requirements. As a consequence,

vicarious calibrations, the so-called Ocean Target Transformation (OTT) for SMOS (Yin et al., 2013) and Ocean Target Calibration (OTC) (Meissner et al., 2018) for Aquarius and SMAP, are applied for removing spatially homogeneous but time-varying biases in the measured minus expected radiometric signal. OTT is computed in a limited region, almost free of RFIs and land sea contamination, while OTC is estimated from global comparisons. The SSS references come from either a climatology (SMOS), an ocean model (SMAP) or an Argo-derived field (Aquarius), the choice being partly driven by the reference product availability with respect to production temporal constraints. In addition, a latitudinal seasonal varying correction for the SMAP antenna emissivity is derived for each day of the year from Scripps Argo SSS (Meissner et al., 2019).

The auxiliary geophysical information necessary to initialize the SSS retrieval is a possible source of uncertainty. In the case of SMOS, wind, SST and atmospheric parameters are extracted from the European Center for Medium Weather Forecast (ECMWF) Integrated Forecast System (IFS). In the case of Aquarius and SMAP, atmospheric parameters are extracted from the National Centers for Environmental Prediction (NCEP) General Data Assimilation System (GDAS) and SST is from the Canadian Meteorological Center (CMC). In the future, the Copernicus Microwave Imaging Radiometer (CIMR) (Donlon, 2020)) will provide L-band measurements together with higher frequency data that are sensitive to SST (C-band), and surface roughness (K-band) allowing a more precise initialization of SSS retrieval.

2.3 In situ and model data

2.3.1 ISAS

Monthly gridded fields of salinity derived from in-situ measurements are obtained from the ISAS v6 algorithm, an optimal interpolation (OI) tool (Bretherton et al., 1976) developed for the synthesis of the Argo global dataset (Gaillard et al., 2016). ISAS OI considers spatio-temporal length scales between 300km and 4 times the Rossby radius and between 3 weeks and 1 week. In practice, the smoothing is very dependent on the availability of in situ measurements, with, on average, one Argo measurement every 10 days and every 3°x3° (Roemmich et al., 2019).

We use the ISAS fields reconstructed at 5 m depth on a half degree horizontal grid for two purposes. First, ISAS 2011-2016 latitudinal profiles are qualitatively used for defining the reference across swath location for the SMOS latitudinal seasonal bias correction. Second, at each grid point, a statistical distribution property of ISAS SSS is used to adjust the long-term absolute reference of the CCI L4 SSS corrected fields (see Figure 2 and section 2.4.4). In very variable regions, the SSS statistical distribution is skewed towards low SSS values (e.g. (Bingham et al., 2002)) and these low SSS values are poorly reproduced by gridded in situ salinity products (Fournier and Lee, 2021). Hence, in very variable regions, we adjust the 80% quantile of CCI SSS to that of ISAS one whereas we adjust the medians (50% quantiles) in less variable regions.

2.3.2 Ocean model reanalysis

We estimate the amplitude of the SSS variability at spatio-temporal scales that are not resolved from satellite missions. To that end, we use salinity fields at 0.5 m depth between 2011 and 2014, from the GLORYS eddy resolving (1/12°) global oceanic re-analysis produced by Mercator Ocean. This model re-analysis assimilates satellite sea level anomalies, SST, sea ice concentration, in-situ temperature and salinity vertical profiles (but not satellite SSS) and is forced using climatological runoffs. More information about this product can be found on https://resources.marine.copernicus.eu/?option=com_csw&view=details&product_id=GLOBAL_REANALYSIS_PHY_001_030.

2.4 OI methodology:

We summarize below the basic principle of the OI methodology. A more detailed description is given in supporting information S3.

In order to estimate SSS at a given time, the algorithm uses an OI in the time domain, applied independently to each node of the spatial grid. We do not apply any catch-up to reference climatological fields which might remove or attenuate important interannual and/or large mesoscale variations.

Together with SSS and its associated random uncertainty, the CCI+SSS monthly OI estimates a systematic correction, bc, that is applied to each satellite SSS observation. bc mainly corrects for biases related to land-sea contamination and permanent RFI. The algorithm is very

similar to the one described in (Kolodziejczyk et al., 2016) but applied to different sensors and geometries.

To estimate SSS time series at spatial resolution R1 and temporal resolution T1, knowing that SSSobs are at spatial resolution r1 and temporal resolution t1, the cost function (to be minimized) is written as (for monthly OI):

$$C(SSS, bc) = (SSSobs - F(m))^T.Ct^{-1}.(SSSobs - F(m)) + (m - m\_prior)^T.Cm^{-1}.(m - m\_prior) \quad (2)$$

with:

$$m=\begin{pmatrix} SSS \\ bc \end{pmatrix} \quad \text{and} \quad F(m)=SSS-bc$$

where ^{T} indicates the transpose operator, SSSobs, SSS and bc are respectively vectors containing the observed datasets, the estimated SSS and the estimated biases of the SMOS, SMAP and Aquarius data. m_prior contains the SSS and bc a priori values. For the weekly OI, there is no bias correcteion as the monthly OI is used as an a-priori value, only SSS is estimated (m=SSS). Ct is the observation error covariance matrix containing the expected random errors of the satellite SSS relative to the OI SSS. It includes random uncertainty of the satellite SSS observation, Co, and a representativity uncertainty, Cr, that is added to take into account the difference in resolution of fields (R1;T1) and (r1;t1):

$$Ct=Co+Cr$$

This covariance is seasonally dependent and specific to each grid node.

The a priori error covariance matrix, Cm, contains the random fluctuations allowed around the a priori fields of SSS, σ_{SSS}, and of bc, σ_{bc}. In the monthly OI, SSSprior is constant over time and σ_{SSS} are derived using a monthly climatology of SSS variability. σ_{bc} is set to an arbitrary constant value (chosen equal to 4 pss, a value well above reasonable values for retrieved bc). In case of the weekly OI, SSSprior are taken equal to the monthly L4 SSS and σ_{SSS} are derived from the uncertainties of the monthly L4 SSS estimated by the monthly OI combined with the expected variability between monthly and weekly fields derived from model simulations. The variability fields are seasonally dependent and specific to each grid node.

The solution of the minimization provides the estimated SSS and bc, m_est:

$$m\_est=m\_prior+Cm'\cdot H^T \cdot (H\cdot Cm\cdot H^T+Ct)^{-1} \cdot (SSS_{obs}-F(m\_prior))$$

with H the matrix of the partial derivatives of each sensor SSS relative to the estimated parameters. Cm is the time covariance matrix operating in the observation space and Cm' the

time covariance matrix between the observation space and OI product space. A posteriori uncertainty term, corresponding to L4 SSS random uncertainty, is also derived.

The way we derive the various terms involved in equation (2) is described in the following sections.

2.4.1 Climatology of SSS variability:

We explain below how the information about SSS variability introduced in the Cm matrix is built.

SSS variability is introduced to distinguish between SSS fluctuations due to an instrumental flaw or to a plausible geophysical SSS variation. For instance, in a river plume, during runoff season, the SSS is allowed to fluctuate much more than during calm periods. SSS variability is considered at two temporal scales in the OI:

- the sub-monthly SSS variability combined with interannual SSS variability in each pixel, $SSSvar_{month}$, that is used to estimate monthly SSS, taking a constant SSS value as SSSprior;

- the variability of SSS at 50km/7days relative to SSS at 50km/1month resolution, $SSSvar_{week}$, that is used to estimate weekly SSS, taking monthly SSS as SSSprior.

$SSSvar_{month}$, is estimated on each grid node and for each month of the year, as the root mean square difference, RMSD between satellite SSS for the considered month, and the SSS averaged over all months and all years, *y*, over the whole time period, $\overline{SSS}$:

$$SSSvar_{month}(\phi, \lambda, m)=\sqrt{\frac{\sum_y (SSS(\phi,\lambda,y,m)-\overline{SSS})^2}{Ny}} \text{ with } \overline{SSS} = \frac{\sum_{y,m} SSS(y,m)}{Ny*Nm}$$

Hence the variability is seasonal and SSS is allowed to fluctuate more or less around its mean value with the seasons. To remain as coherent as possible with respect to the variability sampled by the satellite measurements, we prefer to avoid estimating it from model simulations. Instead, we estimate it recursively from satellite SSS fields as follows. In a first step, we estimate this variability from the SMOS filtered SSS in regions that are not strongly contaminated by errors (low to middle latitudes, excluding RFI contaminated areas). In regions where SMOS SSS are very noisy (such as in RFI contaminated areas e.g. close to Fiji island or in the Bay of Biscay,

we artificially set a low variability; at very high latitudes, we consider ISAS SSS variability increased by a factor of 2 in order to leave the possibility of unexpected fluctuations). These monthly variability fields are then used to provide a first estimate of CCI L4 SSS weekly fields. The CCI L4 SSS weekly fields are then used to derive a $SSSvar_{month}$. The use of weekly OI fields instead of individual satellite SSS aims at avoiding too large RMSD values due to outliers (see Figure 3 and supporting information S4).

The monthly SSS variability is the dominant term among the representativity uncertainties between the several spatio-temporal scales involved in the OI and the monthly to weekly variability which will be described below. An example $SSSvar_{month}$ is illustrated on Figure 3 for August. The main regions of high variability include, as expected, river outflow regions (Amazon, Congo, Mississippi, Ganges) and western boundaries (Gulf Stream). Other examples of monthly variabilities used in the OI are provided in supporting information S4.

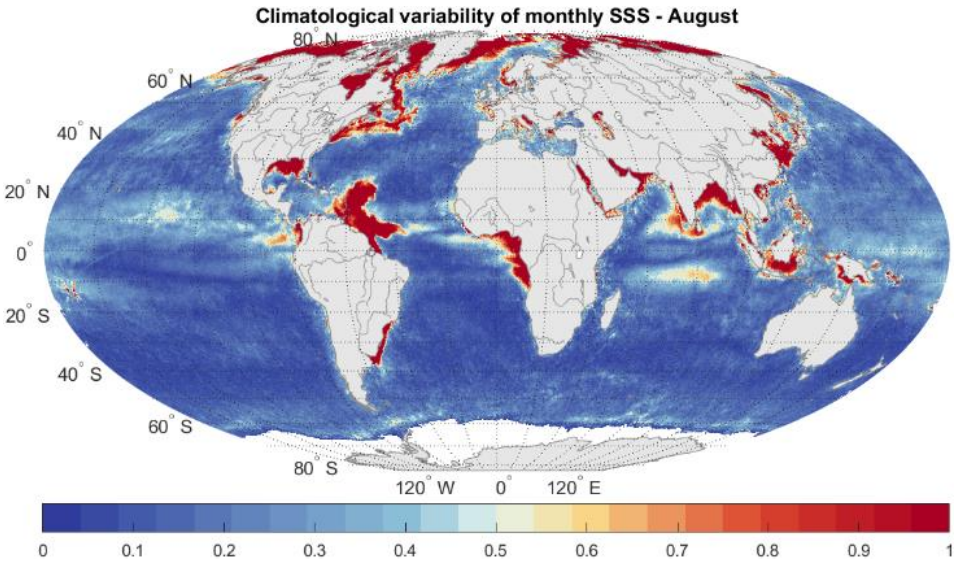

Figure 3: Climatological map of monthly SSS variability in August (August SSS RMSD relative to the SSS averaged over the whole period).

Estimates of the variance of weekly fluctuations relative to the monthly averaged fields are derived from GLORYS simulated SSS. Since river discharges used in the model simulations are based on climatological river runoff information, temporal and spatial variations in river plumes are not properly considered and may be underestimated. We, therefore, take an estimate for this variability defined by twice the RMSD between 50 x 50 km^2 daily and 50 x 50 km^2 30-day mean SSS for each month, obtained from GLORYS fields at $1/12^{th}$ of a degree resolution and then smoothed over space scales of 200 km (see supporting information S5).

2.4.2 Random uncertainties of satellite SSS measurements:

We describe below how the random uncertainties, linked to observational errors (Vinogradova et al., 2019) and reported in the Co matrix are built.

The SMOS processing provides a 'theoretical' random error, E_{SSS_L2}, derived from the Jacobian of Tb relative to SSS and auxiliary parameters, the expected radiometric noise, the expected random errors on auxiliary parameters, and radiative transfer model. A more realistic estimate of the SSS random uncertainty is obtained by multiplying E_{SSS_L2} by the normalized χ of the Bayesian retrieval, χ_N (Boutin et al., 2018).

For SMAP and Aquarius SSS, we derive random uncertainties from self-consistency analyses of the observed SSS as a function of SST. We check that they correspond to a realistic radiometric noise given the SST dependency of Tb derivative with respect to SSS (Yueh et al., 2001). A theoretical uncertainty is derived that is used for our analysis.

For SMAP, we derive empirical uncertainties by comparing collocated retrieved SSS between fore and aft acquisitions. We computed the standard deviation of the difference, STDD, which should be an estimator of the SSS random uncertainty multiplied by $\sqrt{2}$ (assuming that the random uncertainty is the same for aft and fore acquisitions). The STDD is very close to modeled uncertainty with a 0.45K radiometric noise.

For Aquarius, the random uncertainties are derived from comparisons of Aquarius SSS at time t with the Aquarius SSS at time t + 7 days given the 7-day periodicity of this satellite orbit. For that, we assume that SSS in the open ocean does not change significantly during 7 days, so that the STDD relates to the random error (multiplied by $\sqrt{2}$). A fit to the observed random errors is derived as a function of SST (see supporting information S6).

We check the reasonable behavior of estimated random uncertainties, σSSS, by considering the statistical distribution of the centered reduced SSS, namely, SSSc:

$$SSSc = \frac{SSSobs - SSSref}{\sigma SSS} \quad (3)$$

Where SSSobs is the retrieved SSS possibly corrected from systematic errors and SSSref is a reference SSS. We find that the distribution of SSSc is most often close to a Gaussian law with a standard deviation, STD, equal to 1 over the open ocean at distances further than 800 km

from the coast. Closer to the coast, STD(*SSSc*) deviates from 1. Hence, we estimate multiplicative factors, f(dcoast), to be applied to σSSS, for each instrument independently. Since part of this difference can be associated with representativity errors, we quantify STD(*SSSc*) in grid nodes with low spatio-temporal SSS variability, lower than 0.2, as derived from each instrument RMSD. In regions with greater SSS variability, it is likely that representativity errors will make the *SSSc* distribution non-Gaussian and generate outliers. Hence instead of using a criteria on STD(*SSSc*), we prefer to use robust STD, STD* that filters out outliers (STD*(x) is defined as the median(abs(x -median (x)))/0.67; STD*(x) is equal to STD(x) in case of a Gaussian distribution of x). We then adjust f(dcoast) so that STD*(SSSc) becomes close to 1 (see supporting information S6).

2.4.3 Representativity uncertainties:

We explain below how the representativity uncertainties that are reported in the Cr matrix are estimated. They originate from the different samplings of the various sensors and they are also called sampling uncertainties (Vinogradova et al., 2019).

In the monthly OI, we neglect the representativity uncertainty for SMOS and SMAP, that corresponds to the transition from acquisition time (about one second) to monthly resolution (30 days), because, in the majority of cases, SMOS and SMAP random uncertainties, on the order or larger than 0.5, are much larger than their representativity uncertainties. This might be an issue in highly variable regions, such as river plumes but there, the SSS variability is poorly known, and the frequent revisits of SMOS and SMAP in a month should alleviate this issue. Nevertheless, this will be included in a future version. For Aquarius, which has much smaller observational uncertainty and a poorer spatial resolution, the algorithm takes into account the representativity uncertainty. It corresponds to SSS variability at CCI spatio-temporal scales smaller/shorter than those resolved by the Aquarius fields. The aim is to increase the uncertainty associated with Aquarius data by a representativity uncertainty. We estimate it as the STD between SSS fields smoothed over 150 x 150 km^2 and 50 x 50 km^2 which is calculated off-line using GLORYS simulations. This representativity uncertainty depends on the month and increases in highly variable regions (see supporting information S7). In some parts of the ocean, SSS does not vary over large distances and durations: in this case, the representativity uncertainty tends towards 0.

Tests using this representativity uncertainty lead to too smoothed L4 SSS fields particularly in very variable areas suggesting that the representativity uncertainty is not large enough. This might be due, among other reasons, to a spatial variability of SSS underestimated in GLORYS simulations, especially given the limited 2011-2014 time period we considered, as well as to non-Gaussian distribution of SSS not handled by our method. In order to bypass these artifacts and to preserve small scale features detected by satellite data, possibly at the expense of an increased noise of L4 fields, the variability was spatially smoothed and doubled. This rather coarse methodology should be revised in the future.

Representativity uncertainties are generally low (compared to observational uncertainties) for grid nodes in the open ocean but are large near river mouths, in rainy areas, and very dynamical regions (e.g. Gulf Stream).

Close to the coast and near the river mouths, these uncertainties are difficult to assess to a large extent because of the high interannual variability that limits the validity of the statistical approach. These uncertainties can be greater than 1 and becomes dominant in the error budget as they are larger than SSS observational random uncertainties of original L2 satellite data.

2.4.4 Systematic uncertainty:

We describe below how b_c is parametrized and we illustrate how it is retrieved together with SSS.

Systematic uncertainties, the b_c term in equation (2), that depend on the satellite measurements geometry, are retrieved in the course of the monthly OI. Only systematic uncertainties constant over the full time period, which have been shown to be a main source of contamination (e.g. (Kolodziejczyk et al., 2016)), are estimated in the frame of the OI. The amplitude of the systematic uncertainties depends strongly on the sensor passes (ascending or descending), on the satellite pixel location on Earth, and, on the acquisition geometry (e.g., beam number (for Aquarius), across-swath position in the field of view (for SMOS), aft or fore view acquisition (for SMAP)). We assume that land sea contamination biases are constant over time. This is a reasonable assumption given that temporal variations in Tb on land and sea are generally an order of magnitude smaller than the contrast between land and sea Tb. b_c varies as a function of location, instrument and geometry of observation:

$$SSS_{obs}(t, \phi, \lambda, X, x_{orb}) = SSS_0(\phi, \lambda) + SSS_{rel}(t, \phi, \lambda) - b_c(\phi, \lambda, X, x_{orb}) \quad (4)$$

where the notations are as in equation 1 and X accounts for the geometry of observation, and can pertain to different instruments. X corresponds to fore or aft acquisition for SMAP, to across swath location for SMOS and does not vary for Aquarius. Actually, for a given x_{orb}, a pixel at a (ϕ, λ) location is always seen by the same Aquarius antenna; possible biases between the three Aquarius antennas acquisitions are corrected by b_c estimated in different pixels. In a given pixel, b_c varies relatively to the other geometries with respect to a time invariant arbitrary reference SSS, $SSS_0(\phi, \lambda)$. The residuals of SSSobs – SSS_0 + bc correspond to the temporal variations of SSS, adjusted for biases so as to ensure consistency between the temporal variations of the SSS retrieved under various geometries from the various sensors; they are expressed relative to SSS_0 and are called SSS_{rel} (see example on Figure 4ab). b_c are derived through a least square minimization approach, and a series of iterations. SSS_0 is taken as the mean of all satellite SSS. The largest b_c occurs in the vicinity of land for SMOS data. At the end of the correction process, the corrected SSS, SSS_{corr}, is derived from $SSS_{obs}+b_c$ adjusted with a time-invariant shift, ΔSSS_q, derived from an intercomparison of a quantile of the corrected SSS and ISAS SSS (Figure 4d):

$$SSS_{corr} = SSS_{obs} + b_c + \Delta SSS_q \quad (5)$$

In regions with low SSS variability, ΔSSS_q is derived from the 50% quantile (median) and the quantile is increased up to 80% in regions with high SSS variability, where SSS statistical distribution is skewed towards low values which are not well represented in ISAS fields, due to the Argo undersampling and ISAS smoothing.

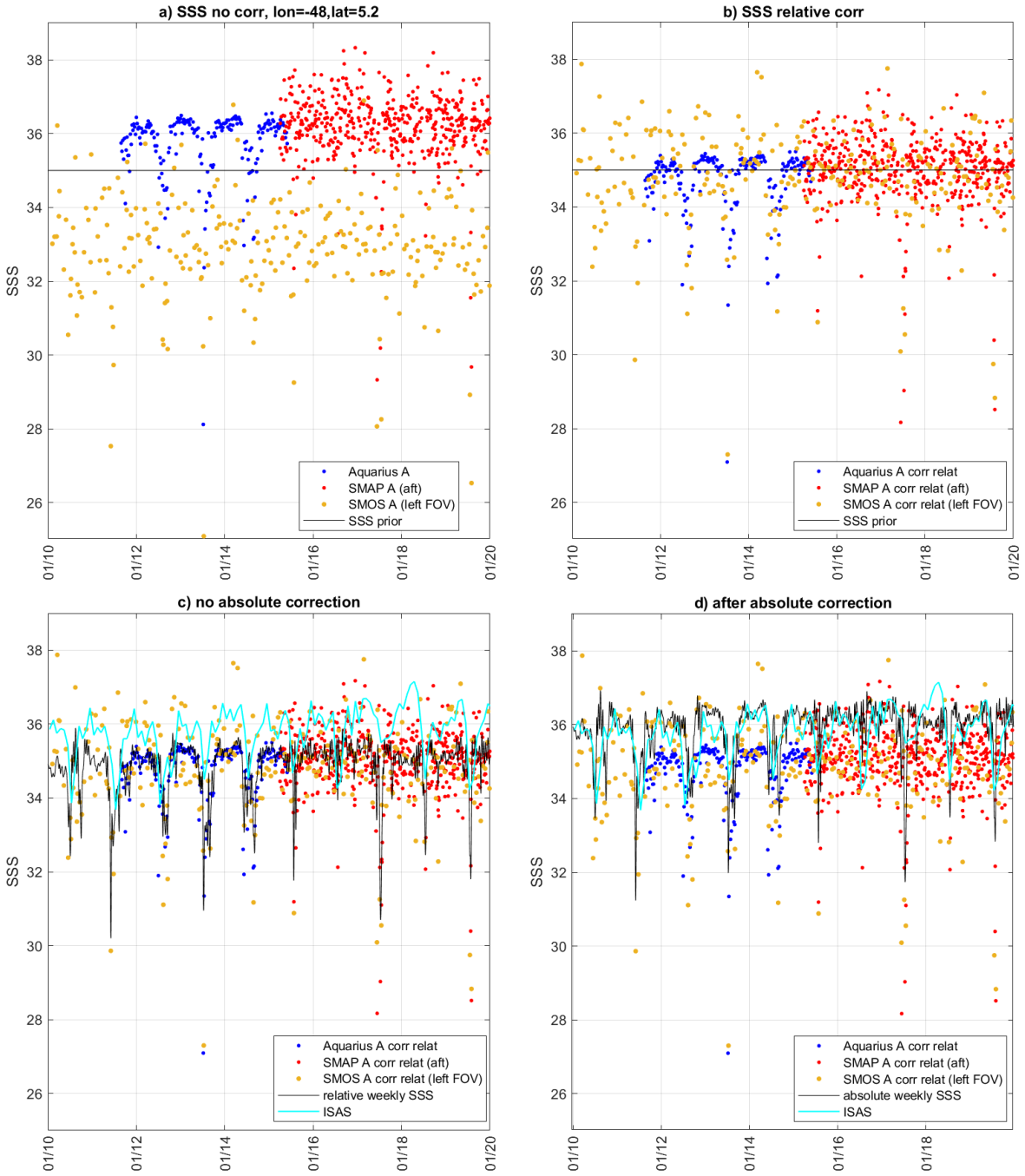

Figure 4: Illustration of the self-consistency approach. Example of a grid point near the Amazon plume (48°W, 5.2°N) affected by land sea contamination, seen under various satellite geometry during ascending orbits (SMOS L2 SSS, left hand side of the FOV, green points; SMAP L2 SSS, aft antenna, red points; Aquarius L3 daily SSS, blue points). a) Satellite SSS before correction (SSS_{obs}) and SSS_{ref} (black line) ; b) Satellite SSS after relative adjustment (SSS_{rel}+SSS_{ref}) and SSS_{ref} (black line); c) Satellite SSS after relative adjustment (SSS_{rel}+SSS_{ref}), weekly OI relative SSS (black) and ISAS SSS (light blue); d) Same as c) but after absolute calibration of the weekly OI SSS by adjusting the 80% quantile of the weekly OI SSS statistical distribution to that of the ISAS SSS.

3 Data and Methods: Validation of CCI L4 SSS

Systematic validations of CCI L4 SSS with respect to various in-situ SSS have been performed by the SMOS Pilot-Mission Exploitation Platform (Pi-MEP). The full PI-MEP comparisons between weekly or monthly CCI+SSS fields and in-situ measurements are available on https://www.salinity-pimep.org/reports/mdb.html. In this paper, we summarize the most striking results, by considering comparisons with in-situ data from Argo profilers, Voluntary Observing Ships (VOS), and Research Vessels (RV).

The differences between satellite and in situ SSS, ΔSSS, are characterized using commonly used L2 norm estimators, arithmetic mean and standard deviation of ΔSSS, STDD. However, representativity errors are likely to generate non-Gaussian statistical distribution of ΔSSS and outliers. In order to minimize these effects, median, STD* (see STD* definition in section 2.4.2) of ΔSSS, STDD*, and the interquartile range, IQR (IQR would be equal to 1.35*STDD in case of a Gaussian distribution of ΔSSS) are also considered as they are expected to better represent satellite SSS errors. We also report the square of the Pearson correlation coefficient, r^2, that indicates the proportion of variance contained in in-situ SSS that is explained by satellite SSS.

To avoid the irregular spatial sampling of Argo matchups (Figure 5), we also report statistics of gridded collocated datasets. In order to keep a significant number of matchups per grid point, the Argo/CCI pairwise MDB is re-gridded on the CCI grid subsampled by a factor of 7 both in latitude and longitude. It corresponds to an Equal Area EASE grid resolution of 175 km. The same bi-weekly temporal sampling as CCI monthly product is conserved. The median value for each grid point of all pairwise MDB values is taken.

We summarize below the characteristics of each dataset and the methodology used to build the matchup data bases (MDB) with CCI L4 SSS.

3.1 Comparisons with Argo SSS:

Argo is a global array of almost 4,000 free-drifting profiling floats that measure temperature and salinity of the upper 2000 m of the ocean. This allows continuous monitoring of the upper ocean conditions, with all data being transmitted by the GTS and made publicly available within 24 hours after collection. The array provides on the order of 100,000 temperature/salinity profiles per year distributed over the global open ocean. Only Argo salinity

and temperature float data with a quality flag set to 1 or 2 and data mode set to real time (RT), adjusted (A), or delayed mode (DM) are considered in Pi-MEP. Argo floats that may have problems with one or more sensors appearing in the grey list maintained at the Coriolis/GDACs are discarded. Furthermore, Pi-MEP provides an additional list of ∼1000 ”suspicious” Argo salinity profiles that are also removed after visual inspection. The upper ocean salinity and temperature values recorded between 0 m and 10 m depth are considered as Argo sea surface salinities (SSS) and sea surface temperatures (SST). These data were collected and made freely available by the international Argo project and the national programs that contribute to it (ARGO, 2020).

The Argo Match-up Data-Base (MDB) is produced from the previously described cleaned Argo dataset. The match-up co-localization temporal window search radius is chosen to select the closest match-up both in time and space, within the spatio-temporal resolution of the satellite fields, i.e. within a spatial radius of 12.5 km around each satellite grid node center and ±7.5 days around the central date of each satellite time step for the monthly CCI L4 SSS products, and ±0.5 days for the weekly ones. If several satellite pixels are found to meet these criteria, the final satellite SSS match-up point is the closest in time from the in-situ data measurement date.

3.2 Comparisons with SSS collected by ship thermosalinograph:

Ship ThermoSalinoGraph (TSG) measurements are sampled at a few kilometres resolution along ship transects, hence, reducing the spatial representativity uncertainty in a satellite pixel with respect to Argo. These higher resolution ‘validation’ data are therefore very useful in very variable regions and the vicinity of land. In this study, we have considered the GOSUD-RV and the LEGOS-DM datasets located mostly at low to mid latitudes, which are very complementary to Argo in high SSS variability regions (Figure 5).

The TSG-GOSUD-Research-vessel dataset corresponds to French research vessels, which have been collecting data since early 2000 as a contribution to the GOSUD program. The set of homogeneous instruments is permanently monitored and regularly calibrated. Water samples are taken daily by the crew and later analyzed in the laboratory. The careful calibration and instrument maintenance, complemented with a rigorous adjustment on water samples lead to reach an accuracy of a few 10^{-2} in salinity. This delayed mode dataset (Kolodziejczyk et al.,

2020) is updated annually and freely available on https://www.seanoe.org/data/00284/39475/ . Adjusted values when available and only collected TSG data that exhibit quality flags 1 or 2 were used.

The TSG-LEGOS-DM dataset is delayed mode data derived from voluntary observing ships collected, validated, archived, and made freely available by the French Sea Surface Salinity Observation Service (Alory et al., 2015). Adjusted values when available and only collected TSG data that exhibit quality flags=1 and 2 were used.

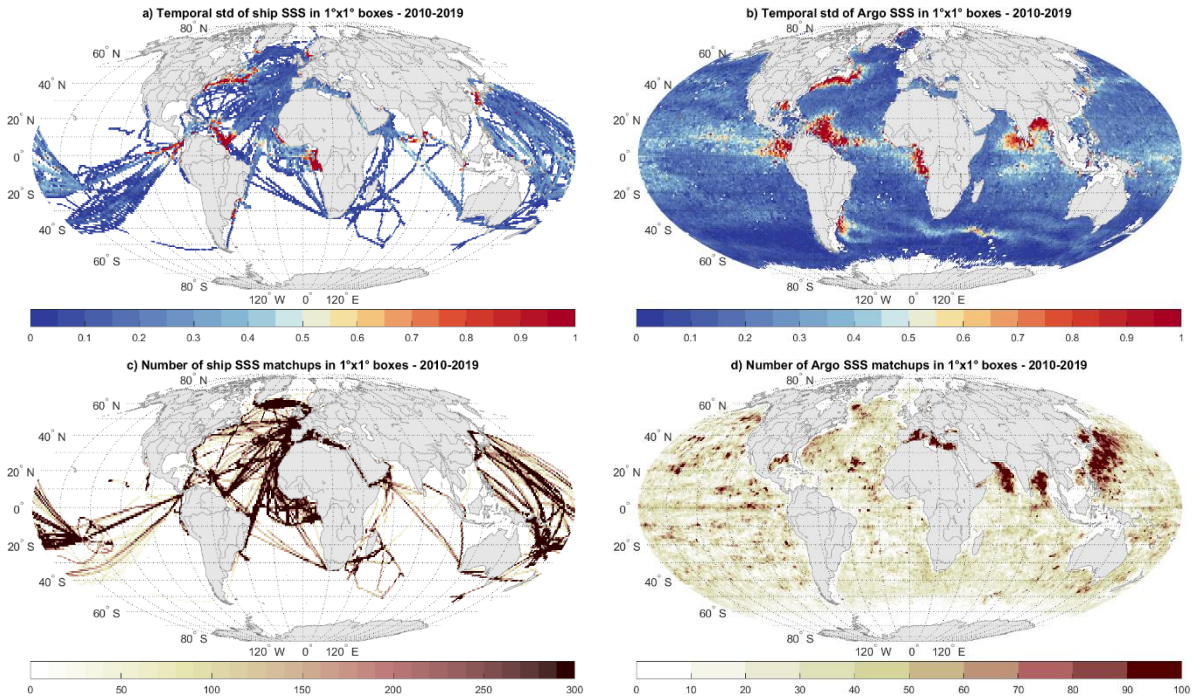

Figure 5: Temporal STD of SSS, in spatial boxes of size 1◦x1◦ as derived from ship TSG (LEGOS DM and GOSUD-Research-vessel) (a), and Argo (b). Number of ship-CCI matchups (c) and Argo-CCI matchups (d). Only match-up pairs with monthly CCI SSS are used to generate these maps.

A spatial smoothing (running median filter with a window width of 25 km) is applied to TSG data before co-locating TSG with CCI L4 SSS, in order to reduce the spatial representativity error.

Each TSG smoothed data is then co-located with all CCI L4 SSS data within a radius of 12.5 km and +/-15 days (for the monthly CCI product) from the TSG data location. If several satellite SSS pixels meet these criteria, the final satellite SSS match-up pixel is selected as the CCI L4 SSS whose central time is closest to the TSG measurement date.

4 Results

4.1 Overview of large scale SSS variability

The ten year-long CCI L4 SSS time series include large scale SSS anomalies, as shown by quarterly SSS anomalies (Figure 6). These SSS anomalies are particularly large in the tropical and subtropical bands and are detected with great realism as indicated by ISAS derived SSS anomalies (see supporting information S8). This comparison is fully independent as no information about interannual SSS variability in ISAS is introduced in the CCI+SSS OI. In areas strongly affected by rain, the comparison must be considered cautiously as the vertical representativeness of Argo and satellite SSS can contribute to non-negligible measurement differences. We shortly recall below the extreme events which occurred during this period and contributed to the main large-scale patterns of SSS variability. In the Pacific ocean, the 2010 and 2011 La Niña events generated strong anomalies in the western equatorial region (Hasson et al., 2014) followed by positive anomalies under the South Pacific Convergence Zone in 2011 and 2012. The 2015-2016 extreme El Niño event first generated large negative anomalies in the equatorial region (Gasparin and Roemmich, 2016; Guimbard et al., 2017) which extended from the eastern Pacific fresh pool to the west of the basin, and which were further advected towards ~25°N (Hasson et al., 2018). In the tropical Indian Ocean, main large scale anomalies are associated with the Indian Ocean Dipole as first evidenced by (Durand et al., 2013). Also noticeable is the interannual variability of the large river plumes (Amazon, Congo, Niger…) where satellite datasets have been shown to better detect variability associated with strong river discharges than in-situ gridded datasets (Fournier and Lee, 2021; Grodsky and Carton, 2018), providing a useful tool for a better understanding of interannual variability related to interactions between fresh plumes and ocean circulation (Akhil et al., 2020).

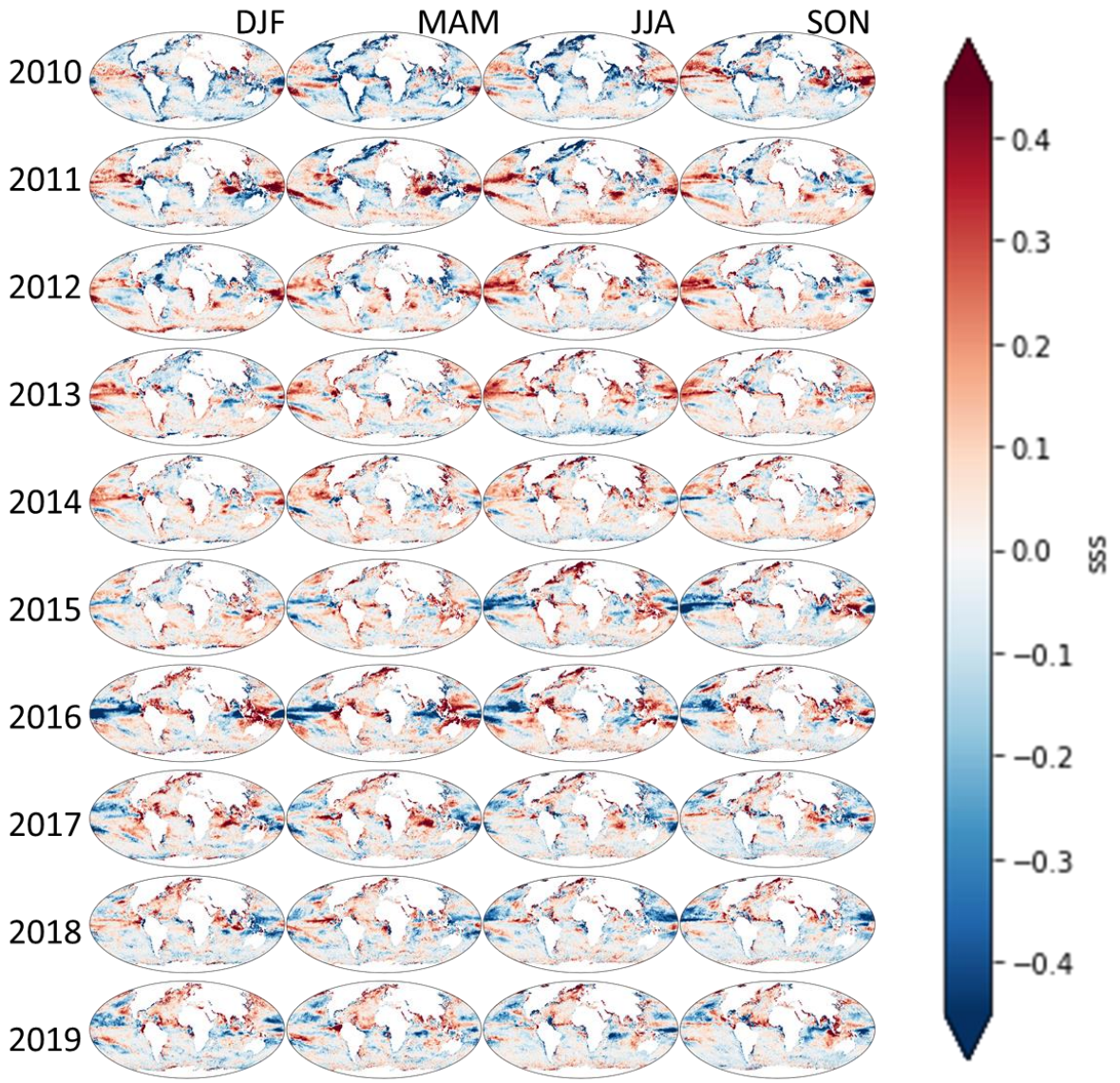

Figure 6: Quaterly SSS anomalies derived from L4 CCI SSS.

4.2 Comparisons with in-situ SSS:

The statistics of the comparisons between monthly CCI SSS and in-situ SSS are reported in Table 3 to Table 6; the ones for weekly SSS are reported in the supporting information S9.

Over the global Ocean, when considering all matchups of monthly (weekly) CCI SSS with Argo SSS, STDD* is 0.16 (0.17), STDD is 0.27 (0.28), r^2 is 0.97 (0.97) (Table 3). When considering only match-up pairs acquired with no Rain Rate (RR) at in situ measurement time (RR=0 mm/h) collected at moderate 10 m height wind speed, 3<U10 <12 m/s, over SST>5°C, and away from coasts, > 800 km (case C1 in PI-MEP; Table 4), the STDD* decreases to 0.13

(0.14), the STDD to 0.16 (0.17) and r^2 is 0.97(0.97). These metrics are amongst the best performance of satellite-Argo comparisons made at the PI-MEP (Table 3 & Table 4).

Table 3: Statistics of monthly satellite SSS comparisons with Argo SSS (All matchups; notice that Aquarius L4 IPRC is adjusted monthly using Argo information)

Statistics of ΔSSS (Satellite - Argo) - ALL

Satellite products	#	Median	Mean	STD	RMS	IQR	r^2	STD*
All period								
smos-l3-catds-locean-v5-18d	1269474	0.01	0.01	0.32	0.32	0.28	0.974	0.21
cci-l4-esa-merged-oi-v2.31-30dr	889299	0.00	0.00	0.27	0.27	0.21	0.969	0.16
SMOS+Aquarius period								
aquarius-l3-or-v5-1m	391630	-0.04	-0.09	0.47	0.48	0.28	0.899	0.21
aquarius-l3-jpl-v5-1m	368837	0.06	0.07	0.30	0.31	0.28	0.922	0.21
aquarius-l4-iprc-v5-1m	372010	0.00	-0.01	0.21	0.21	0.15	0.961	0.11
cci-l4-esa-merged-oi-v2.31-30dr	334414	0.01	0.01	0.28	0.28	0.21	0.961	0.16
SMOS+SMAP period								
smap-l3-rss-v4-1m	604522	-0.02	-0.05	0.39	0.40	0.27	0.980	0.20
smap-l3-jpl-v5.0-1m	614677	0.04	0.02	0.64	0.64	0.35	0.950	0.26
cci-l4-esa-merged-oi-v2.31-30dr	422977	-0.01	0.00	0.25	0.25	0.21	0.980	0.16

Table 4: Statistics of monthly satellite SSS comparisons with Argo SSS (only match-up pairs where RR=0 mm/h, 3<U10 <12 m/s, SST>5°C, distance to coast > 800 km; ; notice that Aquarius L4 IPRC is adjusted monthly using Argo information)

Statistics of ΔSSS (Satellite - Argo) - C1

Satellite products	#	Median	Mean	STD	RMS	IQR	r^2	STD*
All period								
smos-l3-catds-locean-v5-18d	409987	0.01	0.01	0.19	0.20	0.23	0.958	0.17
cci-l4-esa-merged-oi-v2.31-30dr	301849	0.00	0.00	0.16	0.16	0.18	0.970	0.13
SMOS+Aquarius period								
aquarius-l3-or-v5-1m	125302	-0.03	-0.03	0.19	0.19	0.21	0.961	0.16
aquarius-l3-jpl-v5-1m	122877	0.03	0.04	0.19	0.20	0.21	0.962	0.16
aquarius-l4-iprc-v5-1m	122889	0.00	0.00	0.13	0.13	0.13	0.981	0.10
cci-l4-esa-merged-oi-v2.31-30dr	111049	0.00	0.01	0.16	0.16	0.17	0.973	0.13
SMOS+SMAP period								
smap-l3-rss-v4-1m	193751	-0.01	-0.02	0.18	0.18	0.20	0.964	0.15
smap-l3-jpl-v5.0-1m	197243	0.03	0.04	0.24	0.24	0.26	0.938	0.20
cci-l4-esa-merged-oi-v2.31-30dr	144537	-0.01	0.00	0.16	0.16	0.18	0.970	0.13

The large decrease in STDD between All cases and case C1 is in a large part due to the increasing representativity errors between Argo and CCI fields in regions close to land, but could also reflect remaining errors related to land-sea contamination. The statistical comparisons with

Argo exhibit better performances with Aquarius L4 IPRC data likely because the latter are adjusted monthly with Argo SSS, contrary to CCI L4. With respect to the statistical indicators obtained with L3 SSS fields for each individual sensor, the STD and RMS differences with CCI L4 SSS are systematically reduced, because of the noise reduction associated with the OI method. r^2 is much improved with respect to the Aquarius L3, especially when considering "All cases". It is reduced when considering only open ocean data (0.95 with Aquarius weekly data instead of 0.97 with CCI weekly data) where variability at scales smaller than 100 km is significantly less than when the data are within a distance of 800 km from the nearest coastlines. Comparisons of CCI data with TSG data (Table 5 & Table 6) also show systematic improvement of all statistical indicators with respect to L3 SSS from individual sensors. The Aquarius L4 IPRC SSS still outscores CCI SSS in term of STDD* but not for the STDD and r^2 for all cases comparisons: the STDD of CCI SSS with respect to ship TSG SSS is 23% less and r^2 is higher by 16% for monthly CCI L4 SSS compared to Aquarius L4 IPRC SSS (Table 5). This is likely because ship TSGs dominantly explore tropical and mid-latitudes regions (Figure 5) and better sense SSS spatial variability than Argo punctual measurements, in particular in case of extreme values, hence strengthening the better sampling of spatial SSS variability with CCI L4 SSS.

Table 5: Statistics of monthly satellite SSS comparisons with VOS LEGOS DM TSG and GOSUD RV TSG SSS (All matchups)

Statistics of ΔSSS (Satellite - TSG) - ALL

Satellite products	#	Median	Mean	STD	RMS	IQR	r^2	STD*
All period								
smos-l3-catds-locean-v5-18d	9705843	-0.01	0.02	0.64	0.64	0.40	0.882	0.30
cci-l4-esa-merged-oi-v2.31-30dr	5832430	-0.01	0.00	0.48	0.48	0.27	0.870	0.20
SMOS+Aquarius period								
aquarius-l3-or-v5-1m	2461314	-0.13	-0.29	1.22	1.25	0.53	0.484	0.36
aquarius-l3-jpl-v5-1m	2254751	0.07	0.12	0.87	0.88	0.39	0.590	0.29
aquarius-l4-iprc-v5-1m	2220427	0.00	0.08	0.71	0.72	0.22	0.726	0.17
cci-l4-esa-merged-oi-v2.31-30dr	1971061	-0.02	-0.01	0.55	0.55	0.30	0.845	0.22
SMOS+SMAP period								
smap-l3-rss-v4-1m	4817883	0.02	0.09	0.64	0.65	0.36	0.918	0.27
smap-l3-jpl-v5.0-1m	5094655	-0.01	0.00	0.85	0.85	0.40	0.869	0.30
cci-l4-esa-merged-oi-v2.31-30dr	2934792	0.00	0.02	0.41	0.41	0.23	0.901	0.17

Table 6: Statistics of monthly satellite SSS comparisons with VOS LEGOS DM TSG and GOSUD RV TSG SSS (only match-up pairs where RR=0 mm/h, 3<U10 <12 m/s, SST>5°C, distance to coast > 800 km)

Statistics of ΔSSS (Satellite - TSG) - C1

Satellite products	#	Median	Mean	STD	RMS	IQR	r^2	STD*
All period								
smos-l3-catds-locean-v5-18d	1074287	-0.01	0.00	0.20	0.20	0.24	0.959	0.18
cci-l4-esa-merged-oi-v2.31-30dr	798581	-0.01	-0.01	0.18	0.18	0.19	0.968	0.14
SMOS+Aquarius period								
aquarius-l3-or-v5-1m	292990	-0.01	-0.01	0.22	0.22	0.24	0.958	0.18
aquarius-l3-jpl-v5-1m	286023	0.03	0.05	0.23	0.24	0.24	0.953	0.18
aquarius-l4-iprc-v5-1m	276580	-0.01	0.00	0.18	0.18	0.18	0.973	0.13
cci-l4-esa-merged-oi-v2.31-30dr	265588	-0.01	0.00	0.18	0.18	0.20	0.968	0.15
SMOS+SMAP period								
smap-l3-rss-v4-1m	545538	-0.01	-0.02	0.18	0.18	0.20	0.969	0.15
smap-l3-jpl-v5.0-1m	560356	0.01	0.02	0.20	0.20	0.25	0.957	0.18
cci-l4-esa-merged-oi-v2.31-30dr	424268	0.00	0.00	0.17	0.17	0.18	0.970	0.14

With a regular sampling (gridded collocated dataset), the CCI statistical indicators improve slightly: the STDD* is 0.15, the STDD is 0.24. This is likely because of the Argo oversampling in regions strongly contaminated by RFIs (e.g., along Asian coasts; Figure 5).

The global pattern of SSS, its variability and the global SSS statistical distribution are consistently observed by both Argo and the CCI+SSS fields (Figure 7). The spatial patterns are especially coherent in the tropics. At higher latitudes, the CCI+SSS variability in very dynamical regions (Gulf Stream, Agulhas current, Rio De La Plata river plume) appears slightly smaller with CCI fields than it is with Argo individual measurements, possibly due to variability at smaller spatio-temporal scale than 50 x 50 km^2 and one month. On the opposite, the CCI product variability is larger in regions with very stable SSS, e.g. in the Southern Ocean, likely a result of the increasing satellite SSS noise with decreasing temperatures. The statistical distribution of the CCI SSS is close to the one of Argo SSS (Figure 7, bottom left). The statistical distribution of the difference is much narrower than a Gaussian distribution derived from the STDD, and very close to that derived from STDD*, due to the presence of outliers at the edges of the distribution.

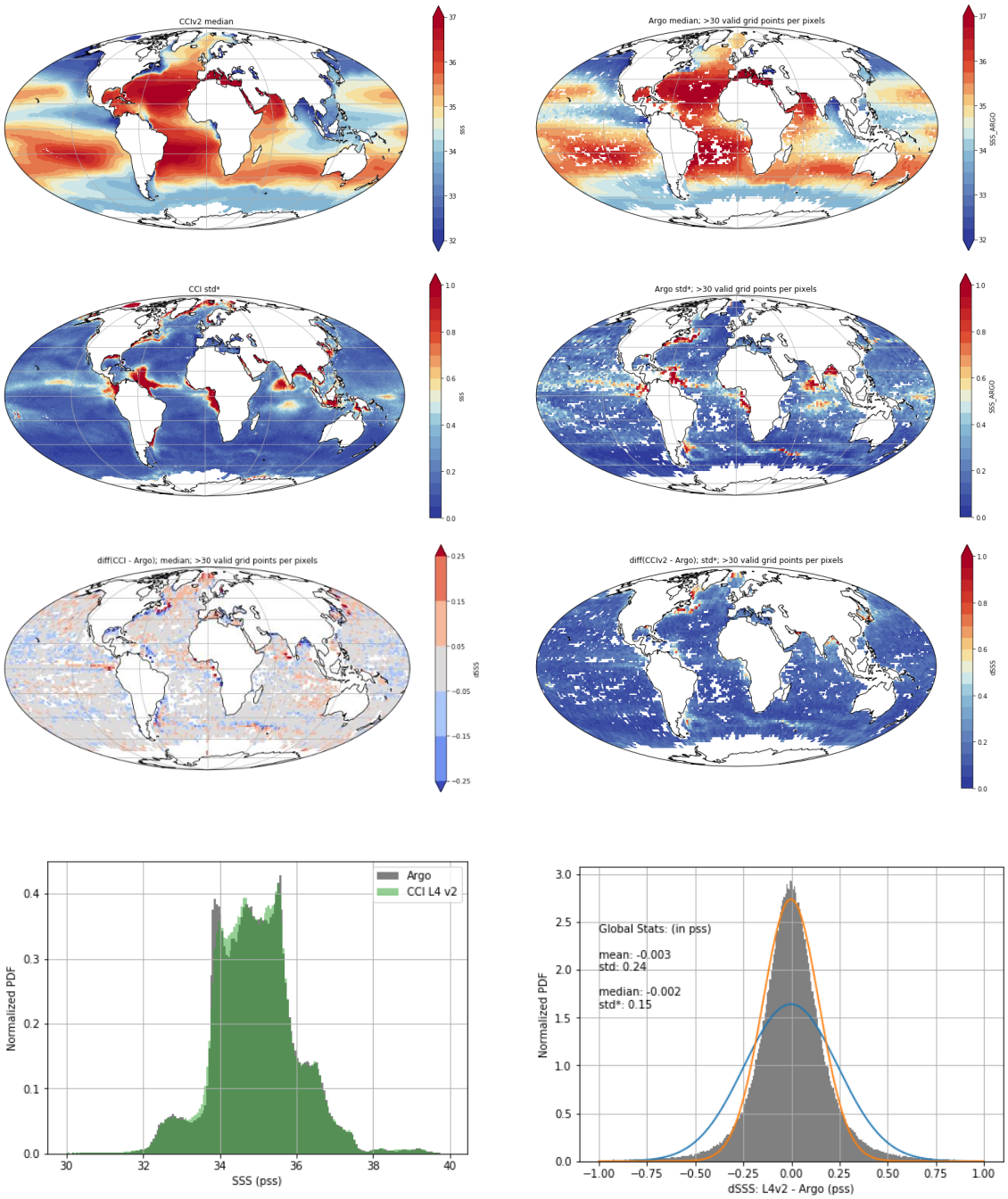

Figure 7: 1st row: Temporal median of (left) CCI L4 and (right) Argo SSS. 2nd row: Temporal robust standard deviation of (left) CCI SSS and (right) Argo SSS; 3rd row: Temporal median (left) and robust standard deviation (right) of gridded pairwise SSS differences between CCI and Argo. 4th row: Histogram of all pairwise gridded data (left) Argo SSS in grey and CCI L4 v2 in light green (regions where Argo and CCI L4 histograms overlap are plotted in dark green); (right) CCI L4 v2 minus Argo difference, (blue line) normal pdf using computed mean and STDD, (orange curve) normal pdf using computed median and STDD*.

It is interesting to consider the temporal evolution of the median, STDD and correlation coefficient, r, between CCI and Argo SSS (Figure 8 and Figure 9). STDD* is always less than

0.2 (Figure 8, 3rd panel). The zonal correlation (Figure 9, bottom) is very rarely less than 0.7 and, in the subtropics, it is most of the time larger than 0.95. r values lower than 0.95 in the tropics are attributable to representativity errors because of frequent vertical salinity stratification between 5m depth and the sea surface in rainy regions and in river plumes. After mid-2011, the STDD decreases, and r increases, due to the inclusion of Aquarius SSS in the OI. Before mid-2015, the median difference varies seasonally pointing out some limitations of our method concerning both Aquarius and SMOS corrections. Our method focused on the correction of the largest biases: temporally constant biases mostly related to land sea contamination, and latitudinal seasonal biases observed on SMOS SSS. Some biases remain due to seasonal latitudinal variations of Aquarius SSS (Kao et al., 2018) which were neglected as they are an order of magnitude lower than the ones observed on original SMOS SSS. The remaining seasonal biases in SMOS data happen because they are not fully constant from year to year, likely because the sun contamination varied (the sun emissivity was maximum in 2014-2015) and the RFIs contaminations varied. For instance, the low r values around 25°N (Figure 9) is linked to intermittent RFI contamination in the Oman Gulf. After mid-2015, the seasonal variations of the median differences are much reduced and r is more stable (Figure 8 and Figure 9). This is possibly because the thermal model of the SMAP reflector was empirically adjusted using Argo temporal-latitudinal SSS profiles (Meissner et al., 2018). However, we also noticed that seasonal latitudinal biases in SMOS SSS and RFI contaminations are reduced after 2015 (not shown). Indeed, the largest differences are observed at high latitudes in cold waters where the sensitivity of radiometric L-band measurements to SSS is reduced, where the correction for roughness effects is very challenging, where the effect of the transitions into and out of the solar eclipse is the largest (in boreal winter above 47°N for SMOS descending orbits) and where sea ice possibly contaminates satellite SSS. Nevertheless, in the Southern Ocean (south of 50°S), the relatively low zonal r values are mainly due to the fact that the zonal SSS variability is lower there than at higher latitude. Actually, STDD and RMSD obtained with the CCI+SSS dataset in the Southern Ocean are of the same order as the global scale values, and in many cases a factor 2 to 3 better than the STDD and RMSD obtained with the original level 3 SSS (Supplementary Information S10).

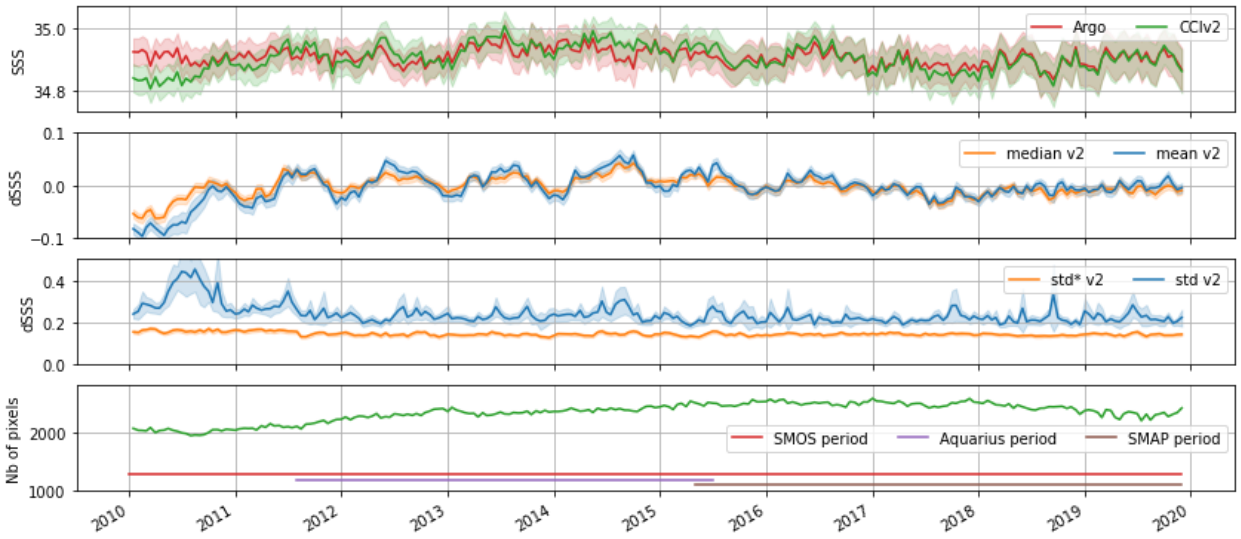

Figure 8: (1st panel): SSS mean of gridded pairwise Argo in red and L4 CCI SSS in green; (2nd panel) Average of; (3rd panel) standard deviation of; the gridded pairwise SSS difference between CCI and Argo SSS. Blue and black dashed lines represent (2nd panel) the mean and (3rd panel) the standard deviation. Orange and solid black lines represent (2nd panel) the median and (3rd panel) the robust standard deviation. The shading indicates the 95% confidence interval.(4th panel): Number of gridded pairwise Argo and L4 CCI SSS and bar chars of SMOS, Aquarius and SMAP periods.

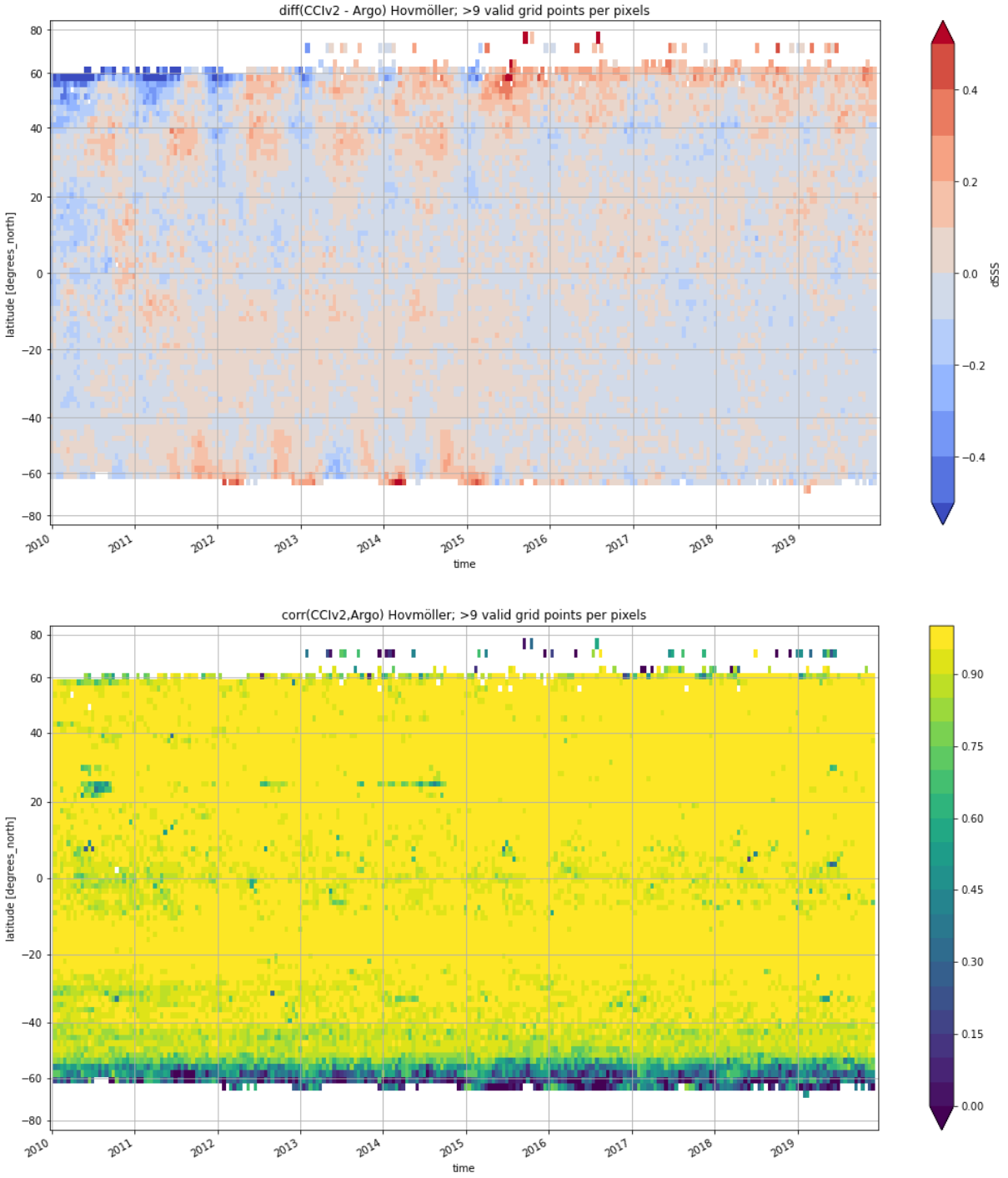

Figure 9: Global latitude-time Hovmöller of (top) the zonally averaged gridded pairwise CCI SSS difference with Argo SSS and (bottom) zonal correlation between gridded pairwise CCI and Argo SSS.

5 Discussion and Perspectives

For the first time, SSS measurements from the three L-band satellite sensors have been merged to produce CCI L4 SSS time series over a decade over the global ocean. No spatial smoothing nor temporal relaxation to in-situ SSS have been introduced in order to keep as much as possible SSS interannual variability sensed by original SSS satellite measurements. On the other hand, the consistent signal between satellite SSS measured by the various sensors and under various geometries has been used to correct for systematic uncertainties. When compared with in-situ Argo SSS, the STDD* over the global ocean is 0.15 with monthly CCI products, the coefficient of determination is 0.97. These performances outscore the ones obtained with fields built from individual satellite measurements. The 50 x 50 km^2 CCI L4 SSS product provides one of the most realistic measure of SSS in very variable regions. The potential of the CCI L4 dataset for revealing new insights has been demonstrated already by various scientific studies. Focussing on the interannual variability of the SSS in the Bay of Bengal and on the signature of the river plumes, Akhil et al. (2020) found that CCI L4 SSS performed better than SSS retrieved from individual satellite sensors. In the tropical Atlantic Ocean, the CCI L4 SSS allowed to study large seasonal and interannual variability in the respective roles of salinity and temperature on the development of the tropical instability waves (TIWs) and to show that, in the top 60-m of the ocean, salinity and temperature each contribute to about 50% of the TIWs perturbation potential energy (Olivier et al., 2020). CCI L4 SSS is also used to document events of freshwater transport off the coast of Suriname and French Guyana from the shelf to the open ocean in January-March since 2010, showing that such unexpected events occurred in 7 out of 10 years (Reverdin et al., 2021).

The specifications of the CCI fields have been defined based on a poll to which 54 potential users have answered. Their requirements are, for a large part, in line with the ones formulated by other user groups and/or in other contexts, as summarized by the World Meteorological Organization (WMO) (https://www.wmo-sat.info/oscar/variables/view/sea_surface_salinity), or by a former user requirement analysis for future microwave radiometers operating at low frequencies (mainly L-Band) (Kerr et al. 2019). All these studies require an accuracy between 0.1 to 0.3 at spatio-temporal scales greater than 100km and one week (see https://www.wmo-sat.info/oscar/variables/view/sea_surface_salinity). While the spatial and temporal resolution requirements of the users and the previously mentioned

studies are compatible with the Global Climate Observing System (GCOS) Implementation Plan (GCOS-200 (214) ; https://library.wmo.int/doc_num.php?explnum_id=3417), the GCOS uncertainty and stability requirements of 0.01 and 0.001 per decade respectively are an order of magnitude more stringent. These values, the same as the ones for subsurface in-situ data, appear very small compared to the SSS variability and the spatio-temporal undersampling of this variability by in-situ near surface salinity measurements. Even with the increase of measurements associated with the full deployment of the Argo buoy network, in-situ near surface salinity measurements do not allow to reach such accuracy over all regions of the global ocean.

The improved accuracy of the CCI L4 SSS with respect to individual sensor SSS accuracy has been made possible because individual sensor SSS products were already shown to detect consistent variabilities. For instance, D'Addezio and Subrahmanyam (2016) showed that SMOS and Aquarius detect high SSS variability associated with the Agulhas current consistent with Argo SSS, whereas Fournier and Lee (2021) showed very consistent SMOS and SMAP SSS in river plumes areas. Yu et al. (2021) and Bingham et al. (2021) found that SSS annual and semiannual amplitudes are quite well represented over the open ocean by the satellite SSS products considered for building the CCI L4 SSS.

The methodology we have developed for building the CCI L4 dataset aims at preserving the SSS variability globally observed by satellite every few days in footprints integrated over typically 50 x 50 km^2. The bias corrections are mostly based on the consistency between SSS signatures recorded by the various satellite datasets and are considering specific properties of each sensor measurements. External SSS information is considered only for calibrating the long term SSS absolute value and for estimating representativity uncertainties. The CCI+SSS approach is, therefore, upstream of the optimal interpolations which correct satellite SSS biases using in-situ SSS fields on a monthly basis or less, such as (Melnichenko et al., 2016). The CCI+SSS fields could be used as inputs to such method, as was done with SMOS data (Nardelli et al., 2016) or with SMOS and SMAP data (Kolodziejczyk et al., 2020).

Nevertheless, there is still room for improving CCI L4 SSS, their uncertainties and validation. In particular, it would be interesting to reach better stability of the CCI L4 SSS time series.

In particular, seasonal latitudinal differences remain with respect to Argo salinities, mostly before mid-2015. After mid-2015, both the inclusion of SMAP SSS and reduced SMOS SSS latitudinal biases are responsible for the improvement. The reason why SMOS SSS are more stable after mid-2015 is not entirely clear, even though a change in the SMOS calibration mode (warm Noise Injection Radiometer (NIR) calibration after November 2014) likely contributes to this improvement. An uncertainty on the temporal variability of SMOS SSS arises from the current use of SSS climatology in the SMOS OTT region. The interannual variability of the median SSS over the OTT region, as determined from ISAS SSS, reaches +/-0.05 during the 2010-2019 period which could be corrected. The model for the dielectric constant of seawater at L-band in cold water has also been shown to remain an issue (Boutin et al., 2021). This will be corrected in the future CCI L4 SSS release. Another source of uncertainty comes from the varying versions of ECMWF forecast fields used as priors (wind speed, SST) in the SMOS SSS retrieval. The use of the same model version for the reanalyzed fields, such as reanalyses like ERA5, could help stabilize the time series. Last, an ongoing SMOS reprocessing with a revised calibration is more stable (preliminary results) and the level 1 revised algorithm corrects part of the sun contamination at the high northern latitudes. For Aquarius SSS, remaining systematic differences have been found between ascending and descending orbits (Kao et al., 2018; Meissner et al., 2018). We have not considered correcting Aquarius SSS for systematic latitudinal seasonal biases before merging with SMOS SSS, but this should be envisioned in the future. Future studies should also pay more attention to systematic differences arising from the components of the radiative transfer models and of the prior datasets which differ between the processing chains of each of the three sensors.

The development of this CCI L4 version 2 algorithm focused on low to mid latitudes regions where satellite SSS datasets were the most mature. Recent products (Brucker et al., 2014; Olmedo et al., 2018; Supply et al., 2020b; Tang et al., 2018) are nevertheless achieving a useful accuracy for detecting Arctic Ocean freshwater changes (Fournier et al., 2020), changes in river plumes extent (Vazquez-Cuervo et al., 2021) and their relations to wind atmospheric forcing (Tarasenko et al., 2021). Hence keeping the best potentialities demonstrated with the existing datasets associated with the three satellite missions at high latitudes will be another remaining main challenge for the future research and developments of CCI+SSS merging algorithms.

In this CCI product, no correction has been applied for rain effects on SMOS SSS products, because reliable rain estimates at hourly resolution as provided by IMERG, and as required by correction or sorting methods (Supply et al., 2020a; Supply et al., 2018), were not available before 2014, i.e., at the time of this CCI+SSS version 2 development. This effect might be non-negligible, even on monthly SSS estimates in the rainiest regions of the globe and is very likely responsible for zonal r lower than 0.95 in the tropics (Figure 9). In very rainy regions such as the Pacific ITCZ, Boutin et al. (2014) estimated that vertical representativeness mismatch might lead to differences between monthly salinity at a few meters depth and in the first-centimeter depth of up to 0.5 at satellite pixel level (50x50 km^2). Nevertheless, this effect is very patchy, and when averaged over all longitudes, it is mostly less than 0.1, except in very abnormal conditions such as in the second part of 2015, when it reached up to 0.15 in the latitudinal band affected by the freshest anomalies (Supply et al. Ph.D. thesis 2020). During this 2015 abnormal period, modelled salinities at 10 m depth and satellite SSS in the northern tropical Pacific Ocean also differed by this order of magnitude (Hasson et al., 2018). Thus, even though this effect did not hamper the detection of 2015 large scale SSS anomalies, and that an estimate of the freshening at 1 cm depth could also be of interest for air-sea interactions studies, it will be important in future CCI L4 SSS releases to provide an estimate of CCI L4 SSS corrected from the vertical representativeness effect.

Validation with standard statistical indicators such as the ones used in this paper has inherent limitations. For instance, high-resolution fields might appear as having a higher RMS difference with respect to reference fields than lower resolution fields when representativity errors between reference fields and high-resolution fields are important. This effect contributes to some lower RMS difference computed with Aquarius than with CCI L4 SSS. We identified it by looking at r^2, but methodologies such as the ones developed in the high resolution modeling community (Crocker et al., 2020) could be investigated to better quantify the accuracy of high-resolution fields relative to lower resolution fields. Wavenumber spectral analysis, such as the one performed on sea surface height by (Dufau et al., 2016), should also be studied in order to validate dynamical features of SSS at various spatio-temporal scales.

The characterization of SSS variability remains challenging as, on one hand, the combination of in-situ and satellite information remains to be improved (Stammer et al., 2021); and on the other hand, regions with high SSS variability such as the river plumes or strong

surface currents regions are the ones benefiting the most from the satellite information (Tranchant et al., 2019). The statistical distribution of SSS is not expected to be Gaussian (Bingham et al., 2002), especially in regions affected by fresh-water inputs, so that vertical, temporal and spatial representativity errors between in-situ and satellite measurements are not expected to be Gaussian. In particular, the SSS distributions are expected to be skewed towards low SSS values while the higher salinity parts of the SSS distributions are expected to vary much less. This leads us to adopt an adjustment of the full time series of CCI L4 SSS and ISAS SSS in fresh and very variable regions based on a high quantile of their statistical distributions. Nevertheless, the OI assumption of Gaussian errors used here might lead to some drawbacks in fresh regions such as river plumes or rainy areas, e.g., an artificial increase (decrease) of the uncertainty during periods with decreased (increased) variability that are very difficult to quantify given the sparseness of existing in-situ measurements. For the reasons outlined above, the validation of the SSS and its uncertainty estimate is very tricky and requires extended research to go beyond the relatively crude validation presented in this paper.

Finally, we plan future CCI+SSS updates typically once every 18 months. In future versions of the CCI products, in addition to a global product, polar products are foreseen. We also plan to develop several regional products with longer time series than the one presented in this paper by extending the L-band based SSS back in time to 2002 over four large and warm river plume regions (1) Mississippi; (2) Orinoco and Amazon; (3) Niger and Congo and (4) Bay of Bengal. For this, we will complement the observations provided by the suite of L-band sensors using AMSR-E lowest microwave frequency channel data (at 6.9 GHz=C-band and 10.7 GHz=X-band) acquired in warm and strongly contrasted dynamical river plume regions. In such conditions, the small SSS signal contained in C-band radiometer data is improved by differentiating the vertical polarization surface reflectance between the C and X band, minimizing SST and wind effects on the data. Monthly-averaged SSS retrievals using such approaches have been already demonstrated from AMSR-E data for the Amazon plume region (Reul et al., 2009) and HY2-A data for the freshwater runoff near the Yangtze Delta (Song and Wang, 2017). In the future, new missions such as the Copernicus Imaging Microwave Radiometer (Donlon, 2020) and the SMOS-High Resolution mission (Rodríguez-Fernández et al., 2019) will benefit from the methods and approaches pioneered by the SSS-CCI activities and extend the climate record of satellite SSS into the 2040's.

Acknowledgments, Samples, and Data

We thank two anonymous reviewers for their comments. We thank F. Bonjean for careful comments about this manuscript and X. Perrot for his feedbacks about the dataset and very fruitful discussions. SSS CCI datasets are freely available at https://catalogue.ceda.ac.uk/uuid/4ce685bff631459fb2a30faa699f3fc5. The PI-MEP MDB are freely available as NetCDF files at ftp://ftp.ifremer.fr/ifremer/cersat/pimep/diffusion/data/; corresponding validation reports are available on https://pimep.ifremer.fr/diffusion/data/. SMAP salinity data are produced by Remote Sensing Systems and sponsored by the NASA Ocean Salinity Science Team. Data are available at www.remss.com. Aquarius data are available at https://podaac.jpl.nasa.gov/dataset/AQUARIUS_L3_SSS_SMID_ANNUAL_V5. CATDS SSS are available at the CATDS Production Data Center (CPDC), www.catds.fr. ISAS and Glorys fields are taken from (https://catalogue.marine.copernicus.eu/; INSITU_GLO_TS_OA_REP_OBSERVATIONS_013_002 and GLOBAL-REANALYSIS-PHY-001-030 products, respectively). The GOSUD RV dataset is available at https://doi.org/10.17882/39475, the ships of opportunity dataset is available at http://www.legos.obs-mip.fr/observations/sss/datadelivery/dmdata. Argo data are taken from http://www.coriolis.eu.org/. This study was funded by ESA CCI contract 4000123663/18/I-NB.

References

Akhil, V. P., J. Vialard, M. Lengaigne, M. G. Keerthi, J. Boutin, J. L. Vergely, and F. Papa (2020), Bay of Bengal Sea surface salinity variability using a decade of improved SMOS re-processing, *Remote Sensing of Environment*, *248*, 111964, doi:https://doi.org/10.1016/j.rse.2020.111964.

Alory, G., et al. (2015), The French contribution to the voluntary observing ships network of sea surface salinity, *Deep Sea Research Part I: Oceanographic Research Papers*, *105*, 1-18, doi:https://doi.org/10.1016/j.dsr.2015.08.005.

Anguelova, M. D., and P. W. Gaiser (2011), Skin depth at microwave frequencies of sea foam layers with vertical profile of void fraction, *Journal of Geophysical Research: Oceans*, *116*(C11), doi:https://doi.org/10.1029/2011JC007372.

ARGO (2020), Argo float data and metadata from Global Data Assembly Centre (Argo GDAC), *SEANOE*, doi:10.17882/42182.

Arias, M., and SMOS_Ocean_Expert_Support_Laboratories (2016), L2OS v622 Reprocessing Report, *Rep. SO-RP-ARG-GS-0100 Issue:2, available on https://smos.argans.co.uk/docs/technotes/SO-RP-ARG-GS-0100_L2OS_Reprocessing_Report_v2.0_160229.pdf*.

Balaguru, K., G. R. Foltz, L. R. Leung, J. Kaplan, W. Xu, N. Reul, and B. Chapron (2020), Pronounced Impact of Salinity on Rapidly Intensifying Tropical Cyclones, *Bulletin of the American Meteorological Society*, *101*(9), E1497-E1511, doi:10.1175/bams-d-19-0303.1.

Bindoff, N. L., W. W. L. Cheung, and J. A. J.G. Kairo, V.A. Guinder, R.Hallberg, N.Hilmi, N.Jiao, M.S. Karim, L.Levin,S. O'Donoghue, S.R. Purca Cuicapusa, B.Rinkevich,T.Suga, A.Tagliabue, and P.Williamson (2019), Changing Ocean, Marine Ecosystems, and Dependent Communities. In: IPCC Special Report on the Ocean and Cryosphere in a Changing Climate [H.-O. Pörtner, D.C. Roberts, V. Masson-Delmotte, P. Zhai, M. Tignor, E. Poloczanska, K. Mintenbeck, A. Alegría, M. Nicolai, A. Okem, J. Petzold, B. Rama, N.M. Weyer (eds.)]. In press.*Rep*.

Bingham, F. M., S. Brodnitz, and L. Yu (2021), Sea Surface Salinity Seasonal Variability in the Tropics from Satellites, Gridded In Situ Products and Mooring Observations, *Remote Sensing*, *13*(1), 110.

Bingham, F. M., S. D. Howden, and C. J. Koblinsky (2002), Sea surface salinity measurements in the historical database, *Journal of Geophysical Research: Oceans*, *107*(C12), SRF 20-21-SRF 20-10, doi:https://doi.org/10.1029/2000JC000767.

Boutin, J., N. Martin, G. Reverdin, S. Morisset, X. Yin, L. Centurioni, and N. Reul (2014), Sea surface salinity under rain cells: SMOS satellite and in situ drifters observations, *Journal of Geophysical Research: Oceans*, *119*(8), 5533-5545, doi:https://doi.org/10.1002/2014JC010070.

Boutin, J., J.-L. Vergely, E. P. Dinnat, P. Waldteufel, F. D'Amico, N. Reul, A. Supply, and C. Thouvenin-Masson (2021), Correcting Sea Surface Temperature Spurious Effects in Salinity Retrieved From Spaceborne L-Band Radiometer Measurements, *IEEE Transactions on Geoscience and Remote Sensing*, *59*(9), 7256-7269, doi:10.1109/tgrs.2020.3030488.
Boutin, J., J. L. Vergely, S. Marchand, F. D'Amico, A. Hasson, N. Kolodziejczyk, N. Reul, G. Reverdin, and J. Vialard (2018), New SMOS Sea Surface Salinity with reduced systematic errors and improved variability, *Remote Sensing of Environment*, *214*, 115-134, doi:https://doi.org/10.1016/j.rse.2018.05.022.
Bretherton, F. P., R. E. Davis, and C. B. Fandry (1976), A technique for objective analysis and design of oceanographic experiments applied to MODE-73, *Deep Sea Research and Oceanographic Abstracts*, *23*(7), 559-582, doi:https://doi.org/10.1016/0011-7471(76)90001-2.
Brodzik, M. J., B. Billingsley, T. Haran, B. Raup, and M. H. Savoie (2012), EASE-Grid 2.0: Incremental but Significant Improvements for Earth-Gridded Data Sets, *ISPRS International Journal of Geo-Information*, *1*(1), 32-45.
Brown, C. W., J. Boutin, and L. Merlivat (2015), New insights into fCO_2 variability in the tropical eastern Pacific Ocean using SMOS SSS, *Biogeosciences*, *12*(23), 7315-7329, doi:10.5194/bg-12-7315-2015.
Brucker, L., E. P. Dinnat, and L. S. Koenig (2014), Weekly gridded Aquarius L-band radiometer/scatterometer observations and salinity retrievals over the polar regions – Part 2: Initial product analysis, *The Cryosphere*, *8*(3), 915-930, doi:10.5194/tc-8-915-2014.
Carmack, E. C., et al. (2016), Freshwater and its role in the Arctic Marine System: Sources, disposition, storage, export, and physical and biogeochemical consequences in the Arctic and global oceans, *J Geophys Res-Biogeo*, *121*(3), 675-717, doi:10.1002/2015jg003140.
CATDS (2017), CATDS-PDC L3OS 2P - Daily valid ocean salinity values product from SMOS satellite, doi:http://dx.doi.org/10.12770/77edd308-4296-4774-b6f3-5b38301cee18.
Cravatte, S., W. S . Kessler, N. Smith, S. E. Wijffels, and Contributing Authors (2016), First Report of TPOS 2020. GOOS-215, 200 pp. [Available online at http://tpos2020.org/first-report/.] *Rep.*
Crocker, R., J. Maksymczuk, M. Mittermaier, M. Tonani, and C. Pequignet (2020), An approach to the verification of high-resolution ocean models using spatial methods, *Ocean Sci.*, *16*(4), 831-845, doi:10.5194/os-16-831-2020.
D'Addezio, J. M., and B. Subrahmanyam (2016), Sea surface salinity variability in the Agulhas Current region inferred from SMOS and Aquarius, *Remote Sensing of Environment*, *180*, 440-452, doi:https://doi.org/10.1016/j.rse.2016.02.006.
Delcroix, T., M. J. McPhaden, A. Dessier, and Y. Gouriou (2005), Time and space scales for sea surface salinity in the tropical oceans, *Deep Sea Research Part I: Oceanographic Research Papers*, *52*(5), 787-813, doi:https://doi.org/10.1016/j.dsr.2004.11.012.
Dinnat, E. P., D. M. Le Vine, J. Boutin, T. Meissner, and G. Lagerloef (2019), Remote Sensing of Sea Surface Salinity: Comparison of Satellite and In Situ Observations and Impact of Retrieval Parameters, *Remote Sensing*, *11*(7), 750.
Donlon, C. J. (2020), The Copernicus Imaging Microwave Radiometer (CIMR) Mission Requirements Document, v4.0, available from https://esamultimedia.esa.int/docs/EarthObservation/CIMR-MRD-v4.0-20201006_Issued.pdf.
Drushka, K., W. E. Asher, A. T. Jessup, E. J. Thompson, S. Lyer, and D. Clark (2019), Capturing Fresh Layers with the Surface Salinity Profiler, *Oceanography*, *32*.
Dufau, C., M. Orsztynowicz, G. Dibarboure, R. Morrow, and P.-Y. Le Traon (2016), Mesoscale resolution capability of altimetry: Present and future, *Journal of Geophysical Research: Oceans*, *121*(7), 4910-4927, doi:https://doi.org/10.1002/2015JC010904.
Durack, P. J., S. E. Wijffels, and R. J. Matear (2012), Ocean salinities reveal strong global water cycle intensification during 1950 to 2000, *Science*, *336*(6080), 455-458, doi:10.1126/science.1212222.
Durand, F., G. Alory, R. Dussin, and N. Reul (2013), SMOS reveals the signature of Indian Ocean Dipole events, *Ocean Dynamics*, *63*(11), 1203-1212, doi:10.1007/s10236-013-0660-y.
Fine, R. A., D. A. Willey, and F. J. Millero (2017), Global variability and changes in ocean total alkalinity from Aquarius satellite data, *Geophysical Research Letters*, *44*(1), 261-267, doi:https://doi.org/10.1002/2016GL071712.
Foltz, G. R., et al. (2019), The Tropical Atlantic Observing System, *Frontiers in Marine Science*, *6*(206), doi:10.3389/fmars.2019.00206.
Font, J., A. Camps, A. Borges, M. Martín-Neira, J. Boutin, N. Reul, Y. H. Kerr, A. Hahne, and S. Mecklenburg (2010), SMOS: The Challenging Sea Surface Salinity Measurement From Space, *Proceedings of the IEEE*, *98*(5), 649-665.

Fournier, S., and T. Lee (2021), Seasonal and Interannual Variability of Sea Surface Salinity Near Major River Mouths of the World Ocean Inferred from Gridded Satellite and In-Situ Salinity Products, *Remote Sensing*, *13*(4), 728.
Fournier, S., T. Lee, and M. M. Gierach (2016), Seasonal and interannual variations of sea surface salinity associated with the Mississippi River plume observed by SMOS and Aquarius, *Remote Sensing of Environment*, *180*, 431-439, doi:https://doi.org/10.1016/j.rse.2016.02.050.
Fournier, S., T. Lee, X. Wang, T. W. K. Armitage, O. Wang, I. Fukumori, and R. Kwok (2020), Sea Surface Salinity as a Proxy for Arctic Ocean Freshwater Changes, *Journal of Geophysical Research: Oceans*, *125*(7), e2020JC016110, doi:https://doi.org/10.1029/2020JC016110.
Gaillard, F., T. Reynaud, V. Thierry, N. Kolodziejczyk, and K. v. Schuckmann (2016), In Situ–Based Reanalysis of the Global Ocean Temperature and Salinity with ISAS: Variability of the Heat Content and Steric Height, *Journal of Climate*, *29*(4), 1305-1323, doi:10.1175/jcli-d-15-0028.1.
Gasparin, F., and D. Roemmich (2016), The strong freshwater anomaly during the onset of the 2015/2016 El Niño, *Geophysical Research Letters*, *43*(12), 6452-6460, doi:https://doi.org/10.1002/2016GL069542.
Grodsky, S. A., and J. A. Carton (2018), Delayed and Quasi-Synchronous Response of Tropical Atlantic Surface Salinity to Rainfall, *Journal of Geophysical Research: Oceans*, *123*(8), 5971-5985, doi:https://doi.org/10.1029/2018JC013915.
Guimbard, S., N. Reul, B. Chapron, M. Umbert, and C. Maes (2017), Seasonal and interannual variability of the Eastern Tropical Pacific Fresh Pool, *Journal of Geophysical Research: Oceans*, *122*(3), 1749-1771, doi:https://doi.org/10.1002/2016JC012130.
Hackert, E., R. M. Kovach, A. Molod, G. Vernieres, A. Borovikov, J. Marshak, and Y. Chang (2020), Satellite Sea Surface Salinity Observations Impact on El Niño/Southern Oscillation Predictions: Case Studies From the NASA GEOS Seasonal Forecast System, *Journal of Geophysical Research: Oceans*, *125*(4), e2019JC015788, doi:10.1029/2019jc015788.
Hasson, A., T. Delcroix, J. Boutin, R. Dussin, and J. Ballabrera-Poy (2014), Analyzing the 2010–2011 La Niña signature in the tropical Pacific sea surface salinity using in situ data, SMOS observations, and a numerical simulation, *Journal of Geophysical Research: Oceans*, *119*(6), 3855-3867, doi:https://doi.org/10.1002/2013JC009388.
Hasson, A., J. T. Farrar, J. Boutin, F. Bingham, and T. Lee (2019), Intraseasonal Variability of Surface Salinity in the Eastern Tropical Pacific Associated With Mesoscale Eddies, *Journal of Geophysical Research: Oceans*, *124*(4), 2861-2875, doi:https://doi.org/10.1029/2018JC014175.
Hasson, A., M. Puy, J. Boutin, E. Guilyardi, and R. Morrow (2018), Northward Pathway Across the Tropical North Pacific Ocean Revealed by Surface Salinity: How do El Niño Anomalies Reach Hawaii?, *Journal of Geophysical Research: Oceans*, *123*(4), 2697-2715, doi:https://doi.org/10.1002/2017JC013423.
Ho, D. T., and J. J. Schanze (2020), Precipitation-Induced Reduction in Surface Ocean pCO2: Observations From the Eastern Tropical Pacific Ocean, *Geophysical Research Letters*, *47*(15), e2020GL088252, doi:https://doi.org/10.1029/2020GL088252.
Houndegnonto, O. J., N. Kolodziejczyk, C. Maes, B. Bourlès, C. Y. Da-Allada, and N. Reul (2021), Seasonal Variability of Freshwater Plumes in the Eastern Gulf of Guinea as Inferred From Satellite Measurements, *Journal of Geophysical Research: Oceans*, *126*(5), e2020JC017041, doi:https://doi.org/10.1029/2020JC017041.
Huang, M., X. Liang, Y. Zhu, Y. Liu, and R. H. Weisberg (2021), Eddies Connect the Tropical Atlantic Ocean and the Gulf of Mexico, *Geophysical Research Letters*, *48*(4), e2020GL091277, doi:https://doi.org/10.1029/2020GL091277.
Ibánhez, J. S. P., M. Flores, and N. Lefèvre (2017), Collapse of the tropical and subtropical North Atlantic CO2 sink in boreal spring of 2010, *Scientific Reports*, *7*(1), 41694, doi:10.1038/srep41694.
Kao, H.-Y., G. S. E. Lagerloef, T. Lee, O. Melnichenko, T. Meissner, and P. Hacker (2018), Assessment of Aquarius Sea Surface Salinity, *Remote Sens.*, *10(9):1341*.
Kerr, Y., et al. (2019), Low Frequency Passive Microwave User Requirement Consolidation Study, Issue 2,*Rep. SO-TN-CB-GS-0075*, CESBIO, Toulouse, https://mycore.core-cloud.net/index.php/s/Y3tpySnNhI9HWUH.
Kerr, Y., et al. (2010), The SMOS Mission: New Tool for Monitoring Key Elements ofthe Global Water Cycle, *Proceedings of the IEEE*, *98*(5), 666-687.
Klein, L., and C. Swift (1977), An improved model for the dielectric constant of sea water at microwave frequencies, *IEEE Transactions on Antennas and Propagation*, *25*(1), 104-111.
Kolodziejczyk, N., J. Boutin, J.-L. Vergely, S. Marchand, N. Martin, and G. Reverdin (2016), Mitigation of systematic errors in SMOS sea surface salinity, *Remote Sensing of Environment*, *180*, 164-177, doi:https://doi.org/10.1016/j.rse.2016.02.061.

Kolodziejczyk, N., D. Diverres, S. Jacquin, Y. Gouriou, J. Grelet, M. Le Menn, J. Tassel, G. Reverdin, C. Maes, and F. Gaillard (2020), Sea Surface Salinity from French RESearcH Vessels : Delayed mode dataset, annual release, doi:10.17882/39475.
Kolodziejczyk, N., M. Hamon, J. Boutin, J.-L. Vergely, G. Reverdin, A. Supply, and N. Reul (2021), Objective Analysis of SMOS and SMAP Sea Surface Salinity to Reduce Large-Scale and Time-Dependent Biases from Low to High Latitudes, *Journal of Atmospheric and Oceanic Technology*, *38*(3), 405-421, doi:10.1175/jtech-d-20-0093.1.
Kristensen, S. S., N. Skou, S. S. Søbjærg, and J. E. Balling (2019), Developments of RFI Detection Algorithms and Their Application to Future European Spaceborne Systems, paper presented at IGARSS 2019 - 2019 IEEE International Geoscience and Remote Sensing Symposium, 28 July-2 Aug. 2019.
Lagerloef, G., et al. (2008), The Aquarius/SAC-D Mission: Designed to Meet the Salinity Remote-Sensing Challenge, *Oceanography*, *21*.
Land, P. E., et al. (2015), Salinity from Space Unlocks Satellite-Based Assessment of Ocean Acidification, *Environ Sci Technol*, *49*(4), 1987-1994, doi:10.1021/es504849s.
Le Vine, D. M., and P. d. Matthaeis (2014), Aquarius Active/Passive RFI Environment at L-Band, *IEEE Geoscience and Remote Sensing Letters*, *11*(10), 1747-1751.
Lefèvre, N., D. F. Urbano, F. Gallois, and D. Diverrès (2014), Impact of physical processes on the seasonal distribution of the fugacity of CO2 in the western tropical Atlantic, *Journal of Geophysical Research: Oceans*, *119*(2), 646-663, doi:https://doi.org/10.1002/2013JC009248.
Li, L., R. W. Schmitt, C. C. Ummenhofer, and K. B. Karnauskas (2016), North Atlantic salinity as a predictor of Sahel rainfall, *Sci Adv*, *2*(5), e1501588, doi:10.1126/sciadv.1501588.
Lin, X. Q., Y.; Sun, D. (2019), Thermohaline Structures and Heat/Freshwater Transports of Mesoscale Eddies in the Bay of Bengal Observed by Argo and Satellite Data, *Remote Sens.*, *11*, *2989*, doi:https://doi.org/10.3390/rs11242989.
Lique, C. (2015), Arctic sea ice heated from below, *Nat Geosci*, *8*(3), 172-173, doi:10.1038/ngeo2357.
Lukas, R., and E. Lindstrom (1991), The Mixed Layer of the Western Equatorial Pacific-Ocean, *J Geophys Res-Oceans*, *96*, 3343-3357, doi:Doi 10.1029/90jc01951.
McPhaden, M. J., S. E. Zebiak, and M. H. Glantz (2006), ENSO as an Integrating Concept in Earth Science, *Science*, *314*(5806), 1740-1745, doi:doi:10.1126/science.1132588.
Meissner, T., F. J. Wentz, and D. M. Le Vine (2018), The Salinity Retrieval Algorithms for the NASA Aquarius Version 5 and SMAP Version 3 Releases, *Remote Sensing*, *10*(7), 1121.
Meissner, T., F. J. Wentz, A. Manaster, and R. Lindsley (2019), Remote Sensing Systems SMAP Ocean Surface Salinities [Level 2C], Version 4.0 validated release S. R. Remote Sensing Systems, CA, USA. Available online at www.remss.com/missions/smap, doi:10.5067/SMP40-2SOCS
Melnichenko, O., P. Hacker, N. Maximenko, G. Lagerloef, and J. Potemra (2016), Optimum interpolation analysis of Aquarius sea surface salinity, *Journal of Geophysical Research: Oceans*, *121*(1), 602-616, doi:https://doi.org/10.1002/2015JC011343.
Melnichenko, O., P. Hacker, and V. Müller (2021), Observations of Mesoscale Eddies in Satellite SSS and Inferred Eddy Salt Transport, *Remote Sensing*, *13*(2), 315.
Millero, F. J. (2007), The Marine Inorganic Carbon Cycle, *Chemical Reviews*, *107*(2), 308-341, doi:10.1021/cr0503557.
Nardelli, B., R. Droghei, and R. Santoleri (2016), Multi-dimensional interpolation of SMOS sea surface salinity with surface temperature and in situ salinity data, *Remote Sensing of Environment*, *180*, 392-402, doi:https://doi.org/10.1016/j.rse.2015.12.052.
Olivier, L., G. Reverdin, A. Hasson, and J. Boutin (2020), Tropical Instability Waves in the Atlantic Ocean: Investigating the Relative Role of Sea Surface Salinity and Temperature From 2010 to 2018, *Journal of Geophysical Research: Oceans*, *125*(12), e2020JC016641, doi:https://doi.org/10.1029/2020JC016641.
Olmedo, E., C. Gabarró, V. González-Gambau, J. Martínez, J. Ballabrera-Poy, A. Turiel, M. Portabella, S. Fournier, and T. Lee (2018), Seven Years of SMOS Sea Surface Salinity at High Latitudes: Variability in Arctic and Sub-Arctic Regions, *Remote Sensing*, *10*(11), 1772.
Picaut, J., M. Ioualalen, T. Delcroix, F. Masia, R. Murtugudde, and J. Vialard (2001), The oceanic zone of convergence on the eastern edge of the Pacific warm pool: A synthesis of results and implications for El Nino-Southern Oscillation and biogeochemical phenomena, *J Geophys Res-Oceans*, *106*(C2), 2363-2386, doi:Doi 10.1029/2000jc900141.
Piepmeier, J. R., et al. (2017), SMAP L-Band Microwave Radiometer: Instrument Design and First Year on Orbit, *IEEE Transactions on Geoscience and Remote Sensing*, *55*(4), 1954-1966.

Qu, T. D., and J. Y. Yu (2014), ENSO indices from sea surface salinity observed by Aquarius and Argo, *J Oceanogr*, *70*(4), 367-375, doi:10.1007/s10872-014-0238-4.
Reul, N., B. Chapron, S. A. Grodsky, S. Guimbard, V. Kudryavtsev, G. R. Foltz, and K. Balaguru (2021), Satellite Observations of the Sea Surface Salinity Response to Tropical Cyclones, *Geophysical Research Letters*, *48*(1), e2020GL091478, doi:https://doi.org/10.1029/2020GL091478.
Reul, N., B. Chapron, T. Lee, C. Donlon, J. Boutin, and G. Alory (2014), Sea surface salinity structure of the meandering Gulf Stream revealed by SMOS sensor, *Geophysical Research Letters*, *41*(9), 3141-3148, doi:https://doi.org/10.1002/2014GL059215.
Reul, N., et al. (2020), Sea surface salinity estimates from spaceborne L-band radiometers: An overview of the first decade of observation (2010–2019), *Remote Sensing of Environment*, *242*, 111769, doi:https://doi.org/10.1016/j.rse.2020.111769.
Reul, N., S. Saux-Picart, B. Chapron, D. Vandemark, J. Tournadre, and J. Salisbury (2009), Demonstration of ocean surface salinity microwave measurements from space using AMSR-E data over the Amazon plume, *Geophysical Research Letters*, *36*(13), doi:https://doi.org/10.1029/2009GL038860.
Reverdin, G., et al. (2021), Formation and Evolution of a Freshwater Plume in the Northwestern Tropical Atlantic in February 2020, *Journal of Geophysical Research: Oceans*, *126*(4), e2020JC016981, doi:10.1029/2020jc016981.
Rodríguez-Fernández, N. J., et al. (2019), SMOS-HR: A High Resolution L-Band Passive Radiometer for Earth Science and Applications, paper presented at IGARSS 2019 - 2019 IEEE International Geoscience and Remote Sensing Symposium, 28 July-2 Aug. 2019.
Roemmich, D., et al. (2019), On the Future of Argo: A Global, Full-Depth, Multi-Disciplinary Array, *Frontiers in Marine Science*, *6*, doi:ARTN 439
10.3389/fmars.2019.00439.
Salisbury, J., et al. (2015), How Can Present and Future Satellite Missions Support Scientific Studies that Address Ocean Acidification?, *Oceanography*, *28*.
Shenoi, S. S. C., D. Shankar, and S. R. Shetye (2002), Differences in heat budgets of the near-surface Arabian Sea and Bay of Bengal: Implications for the summer monsoon, *Journal of Geophysical Research: Oceans*, *107*(C6), 5-1-5-14, doi:https://doi.org/10.1029/2000JC000679.
Siedler, G., J. Church, and J. Gould (2001), *Ocean Circulation and Climate, Observing and modelling the global ocean*, 715 pp., Academic Press.
Soldo, Y., D. Le Vine, and P. de Matthaeis (2019), Detection of Residual "Hot Spots" in RFI-Filtered SMAP Data, *Remote Sens.*, *11(24):2935*, doi:10.3390/rs11242935.
Song, Q., and Z. Wang (2017), Sea surface salinity observed from the HY-2A satellite, *2017*, 8, doi:10.18063/som.2017.01.004.
Stammer, D., M. S. Martins, J. Köhler, and A. Köhl (2021), How well do we know ocean salinity and its changes?, *Progress in Oceanography*, *190*, 102478, doi:https://doi.org/10.1016/j.pocean.2020.102478.
Steele, M., J. Morison, W. Ermold, I. Rigor, M. Ortmeyer, and K. Shimada (2004), Circulation of summer Pacific halocline water in the Arctic Ocean, *Journal of Geophysical Research: Oceans*, *109*(C2), doi:https://doi.org/10.1029/2003JC002009.
Supply, A., J. Boutin, G. Reverdin, J.-L. Vergely, and H. Bellenger (2020a), Variability of Satellite Sea Surface Salinity Under Rainfall, in *Satellite Precipitation Measurement: Volume 2*, edited by V. Levizzani, C. Kidd, D. B. Kirschbaum, C. D. Kummerow, K. Nakamura and F. J. Turk, pp. 1155-1176, Springer International Publishing, Cham, doi:10.1007/978-3-030-35798-6_34.
Supply, A., J. Boutin, J.-L. Vergely, N. Kolodziejczyk, G. Reverdin, N. Reul, and A. Tarasenko (2020b), New insights into SMOS sea surface salinity retrievals in the Arctic Ocean, *Remote Sensing of Environment*, *249*, 112027, doi:https://doi.org/10.1016/j.rse.2020.112027.
Supply, A., J. Boutin, J.-L. Vergely, N. Martin, A. Hasson, G. Reverdin, C. Mallet, and N. Viltard (2018), Precipitation Estimates from SMOS Sea-Surface Salinity, *Quarterly Journal of the Royal Meteorological Society*, *144*(S1), 103-119, doi:https://doi.org/10.1002/qj.3110.
Tang, W., S. Yueh, D. Yang, A. Fore, A. Hayashi, T. Lee, S. Fournier, and B. Holt (2018), The Potential and Challenges of Using Soil Moisture Active Passive (SMAP) Sea Surface Salinity to Monitor Arctic Ocean Freshwater Changes, *Remote Sensing*, *10*(6), 869.
Tarasenko, A., A. Supply, N. Kusse-Tiuz, V. Ivanov, M. Makhotin, J. Tournadre, B. Chapron, J. Boutin, N. Kolodziejczyk, and G. Reverdin (2021), Properties of surface water masses in the Laptev and the East Siberian seas in summer 2018 from in situ and satellite data, *Ocean Sci.*, *17*(1), 221-247, doi:10.5194/os-17-221-2021.

Tranchant, B., E. Remy, E. Greiner, and O. Legalloudec (2019), Data assimilation of Soil Moisture and Ocean Salinity (SMOS) observations into the Mercator Ocean operational system: focus on the El Niño 2015 event, *Ocean Sci.*, *15*(3), 543-563, doi:10.5194/os-15-543-2019.
Vazquez-Cuervo, J., C. Gentemann, W. Tang, D. Carroll, H. Zhang, D. Menemenlis, J. Gomez-Valdes, M. Bouali, and M. Steele (2021), Using Saildrones to Validate Arctic Sea-Surface Salinity from the SMAP Satellite and from Ocean Models, *Remote Sensing*, *13*(5), 831.
Vialard, J., and P. Delecluse (1998), An OGCM study for the TOGA decade. Part I: Role of salinity in the physics of the western Pacific fresh pool, *J Phys Oceanogr*, *28*(6), 1071-1088, doi:Doi 10.1175/1520-0485(1998)028<1071:Aosftt>2.0.Co;2.
Vinogradova, N., et al. (2019), Satellite Salinity Observing System: Recent Discoveries and the Way Forward, *Frontiers in Marine Science*, *6*(243), doi:10.3389/fmars.2019.00243.
Yin, X., J. Boutin, and P. Spurgeon (2013), Biases Between Measured and Simulated SMOS Brightness Temperatures Over Ocean: Influence of Sun, *IEEE Journal of Selected Topics in Applied Earth Observations and Remote Sensing*, *6*(3), 1341-1350.
Yu, L., F. M. Bingham, T. Lee, E. P. Dinnat, S. Fournier, O. Melnichenko, W. Tang, and S. H. Yueh (2021), Revisiting the Global Patterns of Seasonal Cycle in Sea Surface Salinity, *Journal of Geophysical Research: Oceans*, *126*(4), e2020JC016789, doi:https://doi.org/10.1029/2020JC016789.
Yu, L., S. A. Josey, F. M. Bingham, and T. Lee (2020), Intensification of the global water cycle and evidence from ocean salinity: a synthesis review, *Ann Ny Acad Sci*, *1472*(1), 76-94, doi:10.1111/nyas.14354.
Yueh, S. H., R. West, W. J. Wilson, F. K. Li, E. G. Njoku, and Y. Rahmat-Samii (2001), Error sources and feasibility for microwave remote sensing of ocean surface salinity, *IEEE Transactions on Geoscience and Remote Sensing*, *39*(5), 1049-1060.
Zhu, J. S., B. H. Huang, R. H. Zhang, Z. Z. Hu, A. Kumar, M. A. Balmaseda, L. Marx, and J. L. Kinter (2014), Salinity anomaly as a trigger for ENSO events, *Scientific Reports*, *4*, doi:ARTN 6821 10.1038/srep06821.